Sensing Without Borders: A Sensing-Centric Handover Scheme for Continuous WiFi Sensing

MENG WANG, Hefei University of Technology, China
JINYANG HUANG*, Hefei University of Technology, China
YUANHAO FENG, The University of Electro-Communications, Japan
FENG-QI CUI, University of Science and Technology of China, China
MENG LI, Hefei University of Technology, China
XIAOKANG ZHOU, Kansai University, Japan
FUSANG ZHANG, Beihang University, China

WiFi has emerged as a promising sensing medium for ubiquitous perception networks due to its widespread deployment, low cost, and device-free sensing capability. While significant progress has been made, most existing systems operate in a standalone manner, with sensing capability tightly coupled to single or fixed multi-device deployments, which inevitably hinders sensing continuity across large areas. In this paper, inspired by pioneering handover mechanisms in communication systems, we propose *ScHO*, a sensing-centric handover scheme that enables continuous WiFi sensing capability across large areas. Specifically, we first design a sensing-centric handover framework tailored for sensing tasks, *e.g.*, wide-ranging fall detection, enabling uninterrupted sensing under centralized network control. By jointly considering user proximity and the sensing signal-to-noise ratio (SSNR), a theoretical model of sensing-centric handover boundary in multi-link sensing scenarios is formulated. We reveal that when multiple sensing links are associated with the same access point, the handover boundaries follow an Apollonian circle determined by the device deployment. To further enhance system stability and reduce handover delay, we design a novel sensing-oriented handover mechanism to mitigate frequent ping-pong handovers caused by SSNR fluctuations in overlapping coverage regions of adjacent nodes. Extensive experiments demonstrate that: (i) *ScHO* supports reliable device transitions with an average handover latency of 1.18 s and an overall failure rate of 25.6%; and (ii) even in a small-scale three-link sensing network, *ScHO* improves sensing quality by 1.67× compared to the single-node approach, while achieving approximately 1.8× higher resource efficiency than the multi-node method.

CCS Concepts: • **Human-centered computing → Ubiquitous and mobile computing systems and tools**.

Additional Key Words and Phrases: WiFi sensing, Sensing-centric Handover, A3-event Trigger, Channel State Information (CSI)

ACM Reference Format:
Meng Wang, Jinyang Huang, Yuanhao Feng, Feng-Qi Cui, Meng Li, Xiaokang Zhou, and Fusang Zhang. 2026. Sensing Without Borders: A Sensing-Centric Handover Scheme for Continuous WiFi Sensing. *Proc. ACM Interact. Mob. Wearable Ubiquitous Technol.* 10, 3, Article 160 (September 2026), 35 pages. https://doi.org/10.1145/3832037

*Corresponding author.

Authors' Contact Information: Meng Wang, Hefei University of Technology, Hefei, Anhui, China, mengw512@mail.hfut.edu.cn; Jinyang Huang, Hefei University of Technology, Hefei, Anhui, China, hjy@hfut.edu.cn; Yuanhao Feng, The University of Electro-Communications, Tokyo, Japan, fengyuanhao@uec.ac.jp; Feng-Qi Cui, University of Science and Technology of China, Hefei, Anhui, China, fengqi_cui@mail.ustc.edu.cn; Meng Li, Hefei University of Technology, Hefei, Anhui, China, mengli@hfut.edu.cn; Xiaokang Zhou, Kansai University, Osaka, Japan, zhou@kansai-u.ac.jp; Fusang Zhang, Beihang University, Beijing, China, fusang@iscas.ac.cn.

ACM 2474-9567/2026/9-ART160
https://doi.org/10.1145/3832037

1 Introduction

WiFi sensing has emerged as a promising paradigm for ubiquitous perception in next-generation networks [8, 23]. With over 19.5 billion WiFi devices deployed worldwide [46], this infrastructure potentially constitutes the world's largest wireless sensing-ready platform [47]. In the vision of beyond 5G (B5G) and 6G networks, modern wireless systems are evolving from dedicated communication platforms to dual-functional infrastructures capable of utilizing radio signals for both data transmission and environmental sensing (Integrated Sensing and Communication, ISAC) [17, 26, 52, 59]. The capability of environmental sensing is expected to provide a wide range of applications in the fields of smart homes [4, 26, 41, 50], healthcare [31, 56], security [30], *etc.*

Although promising progress has been made in WiFi sensing technologies, there still remains a significant gap between the envisioned ubiquity and its actual scale of deployment. Pioneer research primarily focuses on standalone WiFi sensing systems, where sensing capability is tightly coupled to a single node [10, 11, 58] or fixed multi-node deployments [42, 48]. These approaches either rely on fixed user-device associations, where users are expected to stay near a specific WiFi sensor during routine monitoring [10, 11, 58], or indiscriminately activate all available sensing nodes in multi-device scenarios, which may result in unnecessary sensing resource consumption [12, 22, 27, 28, 48]. Therefore, despite their effectiveness in static or controlled environments, they have not considered mobility-induced sensing discontinuity, and lack any mechanism to ensure continuous sensing as users move across sensing regions. For instance, as illustrated in Fig. 1, users in daily life are inherently non-stationary and often traverse the coverage areas of multiple WiFi sensors, *e.g.*, a fall can happen suddenly in any room. Under these circumstances, sensing systems based on isolated or fixed-position sensors are insufficient to provide continuous and ubiquitous sensing across large areas.

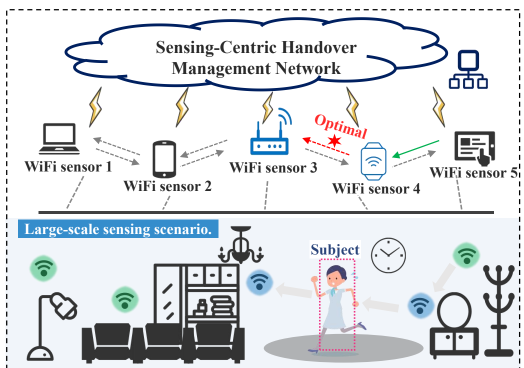

Fig. 1. *ScHO* overview. *ScHO* switches to an optimal WiFi sensor based on sensing quality to enable high-fidelity and uninterrupted sensing services as users traverse different sensing coverage areas.

To bridge this gap, a straightforward solution is to transfer the sensing responsibility among WiFi sensors as users traverse different coverage areas. This echoes the concept of handover (HO) in wireless communications, where an ongoing connection is smoothly transferred between different base stations (BSs) to maintain service continuity [24]. Through timely and seamless switching between links, the handover mechanisms can effectively maintain signal quality and prevent service interruptions. Therefore, to enable continuous sensing in large-scale environments, we introduce a novel **Sensing-centric HandOver** (*ScHO*) scheme that adapts handover paradigms to WiFi sensing. As illustrated in Fig. 1, the basic idea of *ScHO* is to smoothly switch to an optimal WiFi sensor based on sensing quality, so that the sensing service maintains high-fidelity and uninterrupted as users traverse large areas.

However, multiple challenges need to be tackled before this sensing-centric handover scheme can be applied to enable continuous large-scale sensing in WiFi networks.

(1) *How to change the target of the handover scheme for Wi-Fi sensing?* While handover has been extensively studied in communication systems, existing designs primarily focus on maintaining link connectivity and data throughput. In contrast, *ScHO* must explicitly account for sensing performance, which limits the applicability of conventional handover technologies in WiFi sensing scenarios.
(2) *How to design reliable and responsive handover trigger metrics to guide the sensing-centric handover processes?* To enable *ScHO*, one of the key prerequisites is to identify appropriate trigger metrics that determine when a handover should be initiated. Existing state-of-the-art (SOTA) handover trigger metrics are primarily designed for communication purposes, while the triggering metrics for sensing-centric handover that keep sensing tasks continuous and accurate remain unexplored.
(3) *How to minimize handover latency despite the lengthy initialization processes of existing sensing platforms?* Different from communication systems, where link quality is determined instantaneously, sensing quality must be estimated through software processing over a time window with inherent latency. Therefore, how to handle the lengthy initialization delay incurred during sensor switching remains a challenge.

To tackle the aforementioned challenges, we develop a sensing-centric handover system which enables seamless handover across multiple WiFi transmitter-receiver links for continuous WiFi sensing. By seamlessly coordinating WiFi sensors, *ScHO* significantly improves sensing resource efficiency while maintaining comparable performance compared with fully active multi-node sensing. Specifically, our design consists of three key components:

(1) **Centralized Sensing-Oriented Handover Control.** We design a network-controlled sensing-centric handover system to coordinate handover transitions across multiple WiFi sensors. To improve the handover stability, we adopt an anti-shake handover triggering mechanism. By introducing hysteresis thresholds and time-to-trigger (TTT) windows, the designed mechanism effectively filters out instantaneous SSNR fluctuations and significantly reduces the ping-pong effect. We further decouple handover decision-making from edge execution by implementing a centralized plane while retaining sensing operations across distributed WiFi sensors.

(2) **SSNR-based Handover Trigger Metric.** To enable sensing-centric handover decisions, we adapt the sensing signal-to-noise ratio (SSNR) as a mobility-aware, link-level sensing metric, which captures the dynamic variation of sensing quality under user mobility. Building upon SSNR, we develop a unified theoretical framework to characterize sensing-centric handover behavior by modeling the switching boundaries among WiFi sensing links. Through analytical derivation, we reveal that when multiple sensing links are associated with the same access point, the resulting handover boundaries exhibit a clear geometric structure, forming Apollonian circles determined by the relative deployment and configuration of sensing devices. This result provides both theoretical insight and geometric interpretability for sensing-driven handover design.

(3) **Proactive Handover Trigger Mechanism.** To fundamentally mitigate handover latency in device switching, we propose a proactive sensing-centric handover trigger strategy. Specifically, the target device is pre-initialized prior to handover execution to ensure seamless sensing continuity and minimize interruption during handover. This proactive mechanism effectively hides switching delay, significantly reducing handover latency while guaranteeing continuity and smoothness of sensing services during the transition.

To validate the proposed ideas, we implement a real-time ScHO system built upon multiple commodity WiFi sensing nodes and a local-area network (LAN). Extensive experiments conducted in real-world environments demonstrate that the proposed *ScHO* system effectively maintains sensing continuity under user mobility with an overall handover failure rate of 25.6% and an average latency of 1.18 s.

In summary, the main contributions of this work are as follows.

- To the best of our knowledge, we are the first to propose a sensing-centric handover framework, *ScHO*, that enables continuous WiFi sensing under large-area user mobility, achieving scalable, coordinated, and stable sensing performance across multi-node networks with extremely low latency and high sensing performance.

- To support sensing-centric handover decisions, we adopt and validate SSNR as a sensing-aware quality metric, and develop a theoretical handover boundary model that reveals the intrinsic structure of sensing-centric handover behavior under mobility.
- We develop a centralized sensing-centric handover mechanism with an anti-shake triggering to stabilize multi-node sensing coordination under SSNR volatility, and further introduce a proactive triggering scheme to minimize handover latency and sensing interruptions.
- We prototype *ScHO* on a multi-node commodity WiFi sensing testbed comprising three sensing links, and conduct extensive real-world experiments across multiple configurations. Three representative case studies further validate its practical effectiveness, *i.e.*, walking speed estimation, fall detection, and respiration monitoring. Specifically, ScHO achieves a step-frequency MAE of 0.326 Hz, a fall-detection accuracy of 91.12%, and a 38.6% reduction in respiration-rate MAE compared with fixed-link sensing.

2 Background

In this section, we first present the fundamentals of handover mechanisms in mobile communication systems, followed by the basics of WiFi-based human sensing.

2.1 Handover Primer

We start by introducing the background knowledge of Handover (HO). In mobile networks, handover refers to the process of transferring an ongoing connection or service from one base station (BS) to another as the User Equipment (UE) moves across coverage areas. The primary goal of handover is to maintain continuous connectivity and service quality while minimizing interruptions and latency.

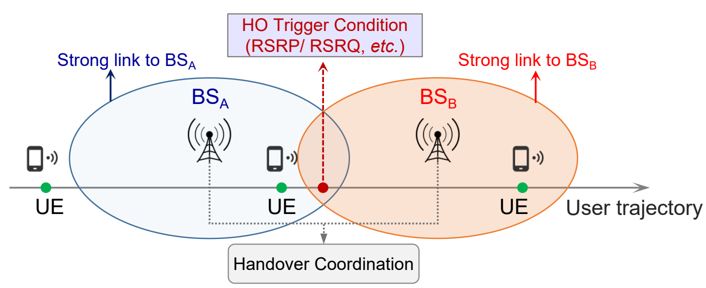

Fig. 2. Communication-oriented handover based on the link quality.

As illustrated in Fig. 2, the handover triggering mechanism primarily relies on signal quality metrics, *e.g.*, RSRP or RSRQ [20, 40], which are continuously monitored by the User Equipment (UE). These parameters are measured both for the serving BS and the neighboring BSs. The handover starts with the *trigger stage* with the serving BS asking the UE for measurements reports of neighbor BSs. After receiving the UE's feedback, the *decision stage* is started, and the serving BS takes the handover decision and identifies the target BS based on the trigger criteria. In the *execution stage*, the serving BS coordinates with the target BS to allocate necessary radio resources, commands the UE to access the new BS, and releases resources upon successful completion. *Overall, the primary objective of communication-oriented handover is to ensure uninterrupted communication services, which can be fundamentally different from sensing-centric handover that prioritizes sensing quality and continuity.*

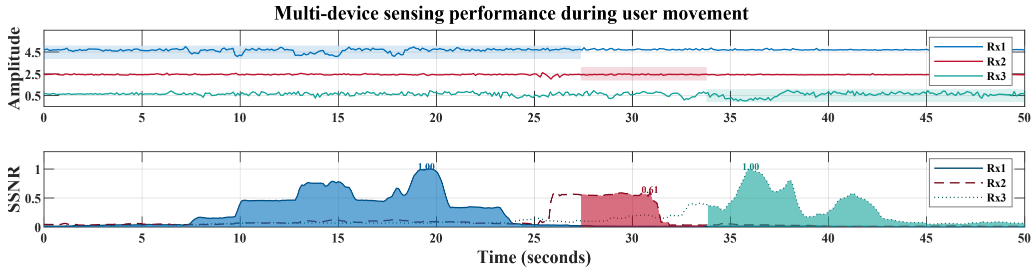

Fig. 3. Illustration of multi-device sensing performance during user movement. With all receivers (Rx1–Rx3) active, only a subset of devices captures significant signal variations at different time instances.

2.2 WiFi Sensing Basics

Consider a general WiFi sensing system with one transmitter (Tx) and multiple receivers (Rxs). The channel gain from the Tx to receiver i can be represented as [54]:

$$\begin{aligned} H_i(f,t) &= H_{s,i}(f,t) + H_{d,i}(f,t) + N_i(f,t) \\ &= |H_{s,i}(f,t)|e^{-j\theta_{s,i}} + |H_{d,i}(f,t)|e^{-j2\pi\frac{d_i(t)}{\lambda}} + N_i(f,t), \end{aligned} \tag{1}$$

where $H_{s,i}(f,t)$ denotes the static channel component for receiver i, $H_{d,i}(f,t)$ denotes the dynamic channel component induced by reflections from the monitored subject $\mathcal{S}$ along the propagation paths from the Tx to receiver i, and $N_i(f,t)$ represents additive noise and interference. The term $e^{-j2\pi\frac{d_i(t)}{\lambda}}$ captures the phase variation of the dynamic path caused by the time-varying path length $d_i(t)$.

To quantify the sensing capability of a WiFi Tx-Rx pair, the sensing-signal-to-noise ratio (SSNR) is defined as the ratio of the dynamic signal power to that of the noise and interference signal, and is defined by [45]:

$$ssnr = \frac{P_d}{P_s + P_n} = \frac{|H_d(f,t)|^2}{|H_s(f,t) + N(f,t)|^2}, \tag{2}$$

where P_s and P_n denote the powers of the static interference and additive noise, respectively. It follows the commonly used SSNR definition in WiFi sensing studies [45], and serves as the link-level sensing-quality indicator in ScHO. In general, a higher SSNR corresponds to better sensing fidelity and reliability, and is more likely to be achieved when the user is closer to the sensing device.

Fig. 3 illustrates the sensing behavior of multiple Tx–Rx links during user movement. When all receivers are active simultaneously, only part of the links exhibit significant dynamic signal variations at a given time, which results in inefficient utilization of sensing resources. As the subject moves across the sensing coverage area, as illustrated in Fig. 4, the sensing quality of different links varies accordingly. Moreover, when the user is in close proximity to a sensing device, the corresponding Tx–Rx link tends to exhibit higher sensing performance.

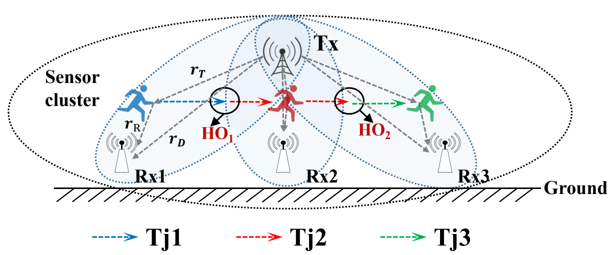

Fig. 4. WiFi-based multi-link sensing scenario under user mobility.

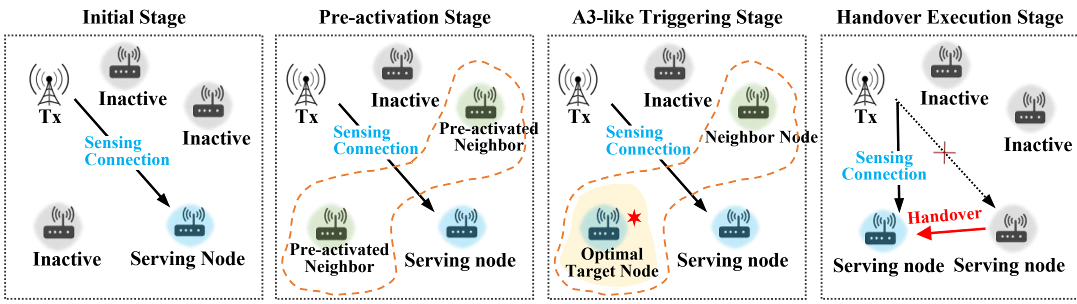

Fig. 5. Illustration of the proposed multi-link *ScHO* mechanism.

Importantly, these links can coexist within the same physical space, indicating that sensing quality varies at the link level rather than the room level. This indicates that many active links do not contribute meaningful sensing information at a given time. Without handover, sustaining sensing performance requires all Tx–Rx links to operate continuously during user mobility, which causes considerable resource redundancy. A large fraction of sensing links remains weakly informative yet actively involved, leading to inefficient utilization of sensing resources and reduced system scalability. This observation highlights the necessity of selectively activating sensing links through handover, rather than maintaining all links concurrently.

3 Theoretical Analysis of Sensing-Centric Handover

3.1 System Model of Sensing-Centric Handover Network

To support *ScHO* across multiple WiFi sensor nodes, we consider a general sensing scenario with multiple WiFi sensors. Since many WiFi devices in real-world deployments (*e.g.*, routers and laptops) are typically stationary or infrequently moved, we assume a quasi-static deployment in which sensing devices remain stationary, while the user is allowed to move freely. The set of receivers associated with a given AP is denoted by $\mathcal{R} = \{s_1, s_2, \ldots, s_m, \ldots, s_M\}$. By connecting to the same AP, multiple receivers aggregate into a sensing cluster, where CSI measurements from the serving and pre-activated candidate receivers are jointly evaluated for sensing-quality comparison. After handover, only the selected serving receiver continues the sensing task.

As illustrated in Fig. 5, the core of the *ScHO* mechanism lies in its dynamic interaction mechanism between these distributed links. Initially, only a single receiver actively performs sensing tasks, while other receivers remain inactive to avoid unnecessary sensing overhead. As the subject moves, neighboring receivers are proactively pre-activated to prepare for potential handover. During this process, the sensing quality of both the serving link and the candidate neighboring links is continuously monitored and compared. When a neighboring link exhibits consistently better sensing quality than the current serving link, a sensing-centric handover is triggered, and the sensing task is smoothly transferred to the optimal target receiver with minimal interruption. More details of the system design can be found in Sec. 4.

However, the above mechanism critically relies on an effective trigger metric to quantify per-link sensing quality and determine when a handover should be initiated. To this end, we introduce an SSNR-based trigger metric in the next subsection.

3.2 SSNR-based Handover Trigger Metric

We use a widely adopted sensing-quality metric, *i.e.*, the Sensing Signal-to-Noise Ratio (SSNR), to quantify the sensing capability of WiFi sensor nodes. It characterizes the ratio between the strength of the sensing-relevant signal and the distortion induced by environmental dynamics. By capturing how sensing performance varies with spatial configurations and user mobility, SSNR provides a unified metric foundation for sensing-centric handover decision-making and theoretical modeling.

Specifically, for a given WiFi Tx-Rx pair, the sensing quality *ssnr* is related to the distance between the transceivers and the distance of the target to the transceivers [45]:

$$ssnr = \frac{P_d}{P_s + P_n} \propto \frac{r_D^2}{(r_T r_R)^2}, \tag{3}$$

where P_d, P_s, and P_n denote the dynamic, static-interference, and noise powers, respectively, r_D, r_T, and r_R are the Tx–Rx and target-to-node distances. It follows the SSNR-geometric relationship established in prior WiFi sensing studies [45], where target mobility is reflected by the time-varying target position. Both the dynamic component P_d and the interference term $P_s + P_n$ inherently include contributions from multipath propagation, where P_d captures motion-induced variations from target-reflected paths, and P_s aggregates static multipath components.

When a single transmitter (AP) serves multiple receivers in an indoor environment, the sensing quality of receiver i at the user position $\boldsymbol{x}$ can be expressed as:

$$q_i(\boldsymbol{x}) \propto \frac{r_{D,i}^2}{r_T^2(\boldsymbol{x})\|\boldsymbol{x} - \boldsymbol{r_i}\|^2}, \tag{4}$$

where $q_i(\boldsymbol{x})$ denotes the sensing quality of i^{th} sensor node at user's position $\boldsymbol{x}$, $r_{D,i}$ denote the distance between the AP and i^{th} sensor node, $r_{T,i}$, and $r_{R,i}$ denote the distance between the target user and AP and the receiver of i^{th} sensor, respectively. The term $\|\boldsymbol{x} - \boldsymbol{r_i}\|^2$ represents the distance from the target to the i^{th} receiver.

Apparently, these formulations show that SSNR is explicitly determined by the spatial geometry among the user, transmitter, and receivers, and thus varies smoothly with user mobility. This enables a direct and consistent comparison of sensing quality across different Tx–Rx links at any location, making SSNR a natural metric for sensing-centric handover decisions. By selecting the link with the highest SSNR, the system can activate the most informative sensing node while suppressing low-utility links, thereby improving sensing continuity and resource efficiency under mobility. Accordingly, we employ SSNR as a mobility-aware sensing quality metric for handover decision-making, while retaining its original formulation from prior work.

3.3 Geometric Characterization of SSNR-Based Handover Boundaries

To further investigate the properties of *ssnr* in handover systems, we analyze the handover boundaries in multi-link WiFi sensing systems. For a given user location, the boundaries between regions are defined by points where two nodes offer equal sensing quality, *i.e.*, $q_i(x) = q_j(x)$. The handover boundary is thus given by:

$$\frac{\mathcal{G}_i \cdot (r_{D,i})^2}{r_T(\boldsymbol{x})^2\|\boldsymbol{x} - \boldsymbol{r_i}\|^2} = \frac{\mathcal{G}_j \cdot (r_{D,j})^2}{r_T(\boldsymbol{x})^2\|\boldsymbol{x} - \boldsymbol{r_j}\|^2}, \tag{5}$$

where $\mathcal{G}_i$ and $\mathcal{G}_j$ denote device-dependent scaling factors that capture hardware heterogeneity (e.g., receiver gain and noise characteristics) for nodes i and j.

As the term $r_T(\boldsymbol{x})^2$ is common to both sides of the equation and does not depend on the sensor nodes, the equation can be simplified as:

$$\frac{\|\boldsymbol{x} - \boldsymbol{r_i}\|^2}{\|\boldsymbol{x} - \boldsymbol{r_j}\|^2} = \kappa_{ij}^2, \qquad \kappa_{ij} \triangleq \frac{r_{D,i}}{r_{D,j}}\sqrt{\frac{\mathcal{G}_i}{\mathcal{G}_j}}, \tag{6}$$

where κ_{ij} is the effective distance ratio between the two sensor nodes, jointly capturing geometric propagation effects and hardware-induced scaling differences. It characterizes how the relative Tx–Rx distances influence the handover boundary between two sensing regions. In particular, a sensor with a longer Tx–Rx line-of-sight distance tends to dominate a larger sensing region. This is consistent with the functional dependence of the handover boundary on κ_{ij}.

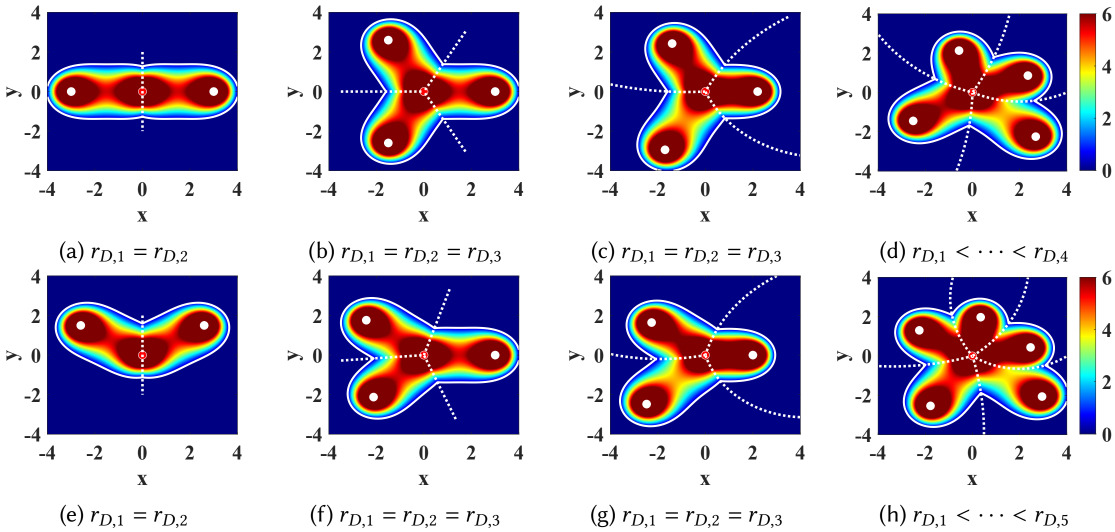

Fig. 6. The heatmap of sensing quality for multiple Tx-Rx pairs. The transmitters are represented by red markers, whereas the receivers are represented by white markers. The dashed lines denote the theoretical boundaries separating the sensing regions of different transceiver pairs.

To simplify the expression, we denote $\boldsymbol{a} = \boldsymbol{r}_i$, $\boldsymbol{b} = \boldsymbol{r}_j$, and $k = \kappa_{ij}$. Therefore, Eq. (6) can be rewritten as:

$$\|\boldsymbol{x} - \boldsymbol{a}\| = k \cdot \|\boldsymbol{x} - \boldsymbol{b}\|, \tag{7}$$

where the distance ratio to the two sensor nodes is constant. As a result, the equation takes the standard form of an Apollonian circle [21]. When $k = 1$, equivalently $\mathcal{G}_i r_{D,i}^2 = \mathcal{G}_j r_{D,j}^2$, the sensing boundary degenerates into the perpendicular bisector of the segment connecting $\boldsymbol{a}$ and $\boldsymbol{b}$.

Based on Apollonian circle geometry [21], the sensing boundary between nodes i and j admits the following closed-form characterization:

$$\begin{cases} c_{ij} = \dfrac{\boldsymbol{a} - k^2\boldsymbol{b}}{1 - k^2}, \\ \rho_{ij} = \dfrac{k\ \|\boldsymbol{a} - \boldsymbol{b}\|}{|1 - k^2|}, \end{cases} \tag{8}$$

where c_{ij} and ρ_{ij} denote the center and radius of the corresponding Apollonian Circle, respectively. The center c_{ij} is located along the line connecting $\boldsymbol{a}$ and $\boldsymbol{b}$, while the radius ρ_{ij} is determined by the receiver separation and the effective distance ratio κ_{ij}, which also accounts for hardware heterogeneity. Importantly, hardware heterogeneity affects the value of κ_{ij} and thus changes the center and radius of the resulting boundary, while the underlying geometric form remains an Apollonian circle.

Fig. 6 visualizes the SSNR heatmaps for multiple Tx–Rx pairs together with the analytically derived sensing boundaries. As we can see, each transceiver pair forms a distinct sensing region whose shape and extent depend on both the Tx–Rx placement and the user's relative position. When the Tx–Rx LoS distances are identical (*i.e.*, $k = 1$, $r_{D,i} = r_{D,j}$), the sensing boundary degenerates into the perpendicular bisector between the two receivers. Otherwise (*i.e.*, $k \neq 1$, $r_{D,i} \neq r_{D,j}$), the boundary forms an Apollonian circle determined by the device deployment. When extended to multi-node scenarios (e.g., 4 or 5 receivers as shown in Fig. 6), the sensing space

Table 1. Typical Handover Triggering Criteria.

Event	Criteria	Explanation
A1	$R_s > \Delta_{A1}$	Serving cell's RSRP is better than a threshold
A2	$R_s < \Delta_{A2}$	Serving cell's RSRP is worse than a threshold
A3 (A6)	$R_n > R_s + \Delta_{A3}$	Neighbor cell is better than the serving cell with an offset
A4 (B1)	$R_n > \Delta_{A4}$	Neighbor cell is better than a threshold
A5 (B2)	$R_s < \Delta^1_{A5}$, $R_n > \Delta^2_{A5}$	Serving cell is worse than a threshold, and neighbor cell is better than a threshold

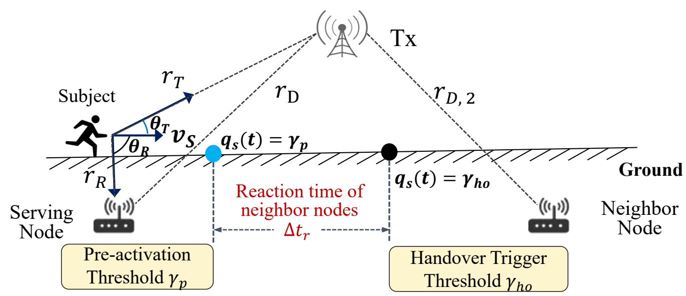

Fig. 7. Handover triggering criteria enabled by proactive pre-activation.

is partitioned into multiple regions through pairwise boundary comparisons among candidate links. Although the overall geometric structure becomes more complex as the number of nodes increases, the underlying principle remains unchanged, where each boundary is still governed by the same Apollonian-circle-based formulation. This boundary corresponds to the locus of points that maintain a constant distance ratio to the two receivers. It provides a theoretical criterion for determining when a handover should occur, i.e., when the sensing quality of two candidate links becomes comparable. In typical sparse or uniform deployments, the receiver closest to the user therefore tends to provide the best sensing performance. This insight lays a solid foundation for designing stable, interpretable, and efficient sensing-oriented handover mechanisms under user mobility.

3.4 Sensing-Centric Handover Triggering Criteria

To bridge the theoretical sensing boundary with a practical handover mechanism, we next derive the triggering criteria for sensing-centric handover. In real-world deployments, sensing measurements are subject to noise, temporal fluctuations, and user mobility, which can lead to unstable handover decisions. Accordingly, we design a proactive triggering mechanism to realize boundary-aware behavior in practice.

As illustrated in Fig. 5, the overall *ScHO* workflow includes the initial, pre-activation, A3-like triggering, and handover execution stages. Within this workflow, the proposed proactive triggering procedure consists of two sequential stages: neighbor-node pre-activation and A3-like triggering. In the first stage, neighboring nodes are proactively activated when the sensing quality of the serving node falls below a pre-handover threshold. In the second stage, *ScHO* verifies the sensing-quality advantage of each pre-activated neighboring node using the A3-like condition and jointly compares all qualified nodes to determine the final handover target.

Stage 1: Neighbor Nodes Pre-activation. As illustrated in Fig. 7, to reduce the handover latency of WiFi sensing systems, the proposed mechanism proactively pre-activates neighboring nodes before handover. Different from communication systems that keep their base stations (BSs) active to maintain connectivity [1, 2], existing

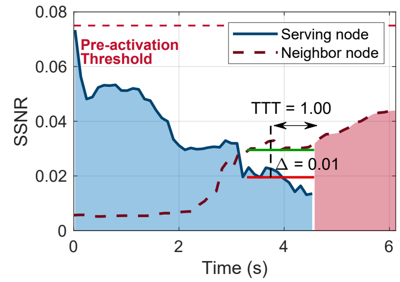

Fig. 8. A3-like handover behavior near the theoretical boundary. Δ provides a boundary buffer, TTT ensures stable transitions, and the pre-activation threshold enables early preparation.

SOTA WiFi sensors try to switch to sensing mode only when a sensing operation is required. This on-demand sensing mechanism inevitably lead to additional handover delays. Therefore, to cope with these delays, we proactively pre-activate the neighbor nodes of the current serving node prior to the handover to enable timely sensing quality evaluation.

During this stage, the serving node maintains the sensing connection, while neighboring nodes begin collecting sensing data in parallel without triggering an immediate handover. Once the sensing quality indicator drops below the pre-activation threshold γ_p, the neighboring nodes begin initialization. The pre-activation trigger condition is given by:

$$q_s(t) \leq \gamma_p, \tag{9}$$

where $q_s(t)$ represents the sensing quality of the serving node, γ_p denotes the pre-activation threshold.

To ensure that neighboring nodes can complete the pre-activation process before the handover condition is satisfied, it is critical to appropriately determine the pre-activation threshold. In particular, the gap between the pre-activation threshold γ_p and the HO trigger threshold γ_{ho} should be sufficient to account for the degradation of $q_s(t)$ during the sensor reaction time Δt_r. Thus, the pre-activation threshold γ_p can be rewritten as:

$$\gamma_p = \gamma_{ho} + \left| q_s\dot{(t)} \right| \cdot \Delta t_r + H, \tag{10}$$

where $q_s\dot{(t)}$ is the degradation rate of sensing quality, H is the hysteresis margin.

The degradation rate $\dot{q}_s(t)$ in Eq. (10) can be obtained by taking the time derivative of $q_s(t)$,

$$\frac{dq_s(t)}{dt} = -2Cr_D^2 \frac{r_R \dot{r}_T + r_T \dot{r}_R}{(r_T r_R)^3} = -2q_s(t) \left(\frac{\dot{r}_T}{r_T} + \frac{\dot{r}_R}{r_R} \right), \tag{11}$$

where $\dot{r}_T$ and $\dot{r}_R$ denote the time derivatives of $r_T(t)$ and $r_R(t)$, respectively. This expression reveals that the degradation rate of the sensing quality is primarily governed by the user's relative motion with respect to the sensing transceiver pair.

Next, we incorporate the mobility of the user into the analysis. During a short time interval, the user velocity v can be approximated as constant. The time derivatives of the transmitter–user and receiver–user distances can be expressed as $\dot{r_T} = v \cos \theta_T$ and $\dot{r_R} = v \cos \theta_R$, respectively. The degradation rate of the sensing quality can be simplified as:

$$\frac{d\, q_s(t)}{dt} = -2q_s(t)v \cdot [\frac{\cos \theta_T}{r_T} + \frac{\cos \theta_R}{r_R}], \tag{12}$$

where θ_T and θ_R denote the angles between the user's moving direction and the transmitter–user and receiver–user vectors, respectively.

To gain further insight into the impact of user mobility on the sensing quality degradation, we consider a simplified motion scenario. Assuming that the user moves directly toward or away from the transceiver pair, the angles θ_T and θ_R can be regarded as negligible (*i.e.*, $\cos\theta_T \approx \cos\theta_R \approx 1$), and the rates of change of the distances can be approximated as $\dot{r}_T \approx \dot{r}_R \approx v$. The degradation rate can then be simplified as:

$$\frac{d\,q_s(t)}{dt} \approx -4q_s(t)\frac{v}{r} \propto -v \cdot \frac{r_D^2}{r^5}. \tag{13}$$

As we can see, the sensing quality degradation rate scales approximately linearly with the user velocity v and inversely with the fifth power of the sensing distance.

Combining Eq. (13) with Eq. (10), the pre-activation threshold can be rewritten as:

$$\gamma_p \approx \gamma_{ho} + 4q_s(t)\frac{v}{r}\Delta t_r + H, \tag{14}$$

where Δt_r denotes the reaction time of neighbor nodes, which involves device initialization, sensing-quality estimation, *etc*.

Based on the pre-activation condition in Eq. (9) and the threshold model in Eq. (14), the relationship between sensing quality and the HO trigger threshold can be derived as:

$$q_s(t)(1 - 4\frac{v}{r}\Delta t_r) \leq \gamma_{ho} + H. \tag{15}$$

When the coefficient $(1 - 4\frac{v}{r}\Delta t_r)$ is positive, an explicit expression for γ_p can be derived. Otherwise, pre-activation under such parameter combinations is challenging, and a more conservative policy should be adopted.

Overall, the neighbor node pre-activation stage plays a critical preparatory role in sensing-centric handover. By proactively initializing neighboring sensing nodes before the actual handover decision, the system creates a temporal buffer that accommodates device initialization, sensing-quality estimation, and SSNR stabilization.

Stage 2: A3-like Handover Trigger Condition. Motivated by the standardized handover principles in 3GPP cellular networks [1], we adopt an A3-like triggering condition for the second stage of the proposed *ScHO* system. Compared with threshold-based events such as A1 and A2, as illustrated in Tab. 1, which only reflect the absolute quality of the serving cell, the A3 event enables a relative comparison between the serving node and its neighbors. This property aligns well with sensing-oriented handover decisions, whose objective is to proactively select a node that offers improved sensing performance. Other neighbor-based events, such as A4 and A5, rely on absolute thresholds on the neighbor quality, or combined threshold conditions on both serving and neighbor nodes. While effective for coverage- and connectivity-driven handover in traditional cellular networks, these events are less suitable for sensing-centric handover, as the sensing performance is scenario-dependent and difficult to characterize using fixed absolute thresholds. Therefore, an A3-like trigger naturally aligns with the sensing-centric handover system, and is adopted as the core triggering mechanism in the second stage of the proposed *ScHO* framework.

The *ScHO* trigger condition is given by:

$$q_n(t) > q_s(t) + \Delta_{A3}, \quad \forall t \in [t_0,\ t_0 + T_{\mathrm{TTT}}], \tag{16}$$

where q_n and q_s denote the sensing quality of the neighboring and serving nodes, respectively, and Δ_{A3} represents a configurable hysteresis margin that controls the sensitivity of the handover decision. For each pre-activated neighboring node, the condition in Eq. (16) is evaluated over the complete time-to-trigger (TTT) interval. A neighboring node is regarded as qualified only when its sensing quality remains higher than that of the serving node by Δ_{A3} throughout this interval.

Fig. 8 shows the A3-like *ScHO* triggering process near the sensing boundary. The solid blue and dashed red curves represent the time-varying SSNRs of the serving and neighboring nodes, respectively. As illustrated, the hysteresis margin Δ_{A3} defines a requisite buffer zone around the boundary. The triggering condition is initially satisfied when the neighbor's SSNR exceeds the serving node's SSNR by this margin. By jointly enforcing a relative SSNR advantage margin and a time-to-trigger (TTT) constraint, the A3-like condition identifies neighboring nodes that demonstrate stable and sustained sensing superiority, rather than transient fluctuations. This temporal-hysteresis design filters out short-term SSNR oscillations caused by environmental dynamics and provides reliable candidates for subsequent target selection.

In a multi-link sensing cluster, multiple neighboring nodes may be qualified simultaneously. In this case, *ScHO* jointly compares all qualified neighboring nodes and selects the final handover target. Let $\mathcal{N}_s$ denote the set of pre-activated neighboring nodes of the current serving node s. The qualified candidate set is defined as $C_s(t_0) = \{i \in \mathcal{N}_s \mid q_i(t) > q_s(t) + \Delta_{A3},\ \forall t \in [t_0, t_0 + T_{\mathrm{TTT}}]\}$. When $C_s(t_0) \neq \emptyset$, the target node is selected according to

$$n^* \in \arg\max_{i \in C_s(t_0)} q_i(t_0 + T_{\mathrm{TTT}})\,. \tag{17}$$

The final comparison selects the optimal available sensing link after temporal filtering. If multiple candidates attain the same maximum sensing quality, a deterministic node order is applied to select a unique target. If $C_s(t_0) = \emptyset$, the current serving node is retained and no handover is performed. The selected target is then passed to the handover execution stage shown in Fig. 5.

To further characterize the scalability of the multi-node handover mechanism, we consider the relationship between the number of sensing links and the time required for coordinated handover. Let Ω denote the sensing area and N denote the number of receiver-associated sensing links. Assuming that the receivers are approximately uniformly deployed and the candidate links have comparable gains, the average area associated with each sensing link can be approximated as $|\Omega|/N$. Using an equal-area circular approximation, the characteristic radius of each sensing region is $r_N \approx \sqrt{|\Omega|/(\pi N)}$, and the corresponding traversal time for a user moving at velocity v is approximately $2r_N/v$.

To complete both neighbor-node reaction and A3-like trigger verification within this interval, $2r_N/v \geq \Delta t_r + T_{\mathrm{TTT}}$ should be satisfied. Combining this condition with the expression for r_N, an area-level estimate of the maximum effectively supported number of sensing links is given by:

$$N \leq N_{\max} = \left\lfloor \frac{4|\Omega|}{\pi v^2 \left(\Delta t_r + T_{\mathrm{TTT}}\right)^2} \right\rfloor, \tag{18}$$

where Δt_r and T_{TTT} denote the neighbor-node reaction time and the A3-like trigger verification interval, respectively. As we can see, $N_{\max}$ increases with the sensing area but decreases with the user velocity and handover preparation time. When N approaches or exceeds this bound, the characteristic traversal time may be insufficient to complete neighbor-node reaction and A3-like trigger verification.

3.5 Proof-of-Concept Experiments

To verify the effectiveness of the proposed *ScHO* framework, we implement a prototype system using commercial WiFi devices and conduct proof-of-concept experiments to validate the feasibility of the proposed system.

Experimental Settings. Our evaluation is conducted in a home environment consisting of two adjacent rooms, *i.e.*, a bedroom and a living room. Two receiver placement strategies are considered: one with both devices located in the same room, and another with devices placed across two rooms. The corresponding user movement trajectories are denoted as Tj_1 (within-room) and Tj_2 (cross-room), respectively. In both cases, the Rxs are positioned sufficiently far apart (*i.e.*, 4 m in the same-room setup and 6 m in the cross-room setup) to ensure distinct sensing perspectives, as illustrated in Fig. 9a and 9d. During testing, each user walks across the two rooms, traversing the sensing coverage areas of both WiFi receivers.

Experimental Observations. Fig. 9 shows the raw CSI amplitude and the normalized SSNR as the user moves across different WiFi sensors' coverage areas. According to the SSNR model proposed in [45], a higher SSNR indicates a better sensing quality. Fig. 9b and 9e show that as the user moves closer to a specific sensing node, the CSI fluctuation and SSNR increase, indicating a higher sensing quality. Conversely, as the user moves away from the current Tx-Rx pair, both CSI fluctuations and SSNR values decline significantly. Notably, this sensing quality

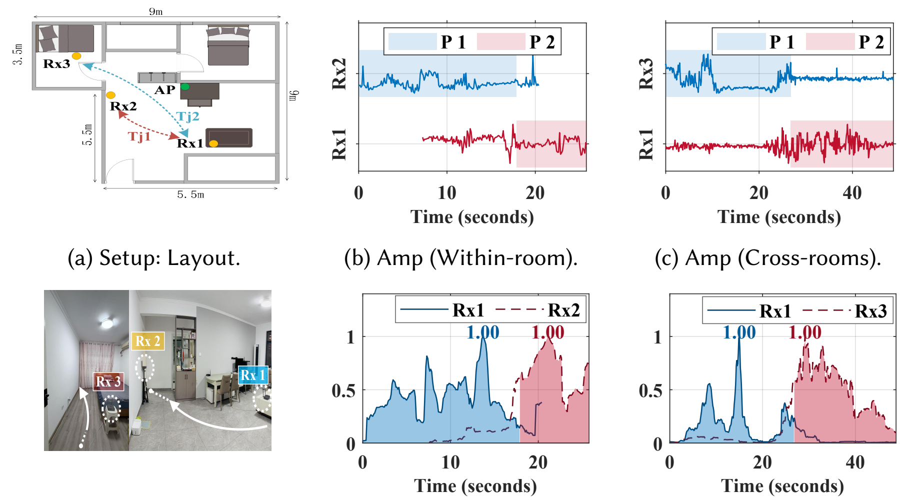

(a) Setup: Layout. (b) Amp (Within-room). (c) Amp (Cross-rooms).

(d) Setup: Deployment. (e) SSNR (Within-room). (f) SSNR (Cross-rooms).

Fig. 9. Proof of concept experiments. (a) (d) experimental setup showing layout and deployment; (b, c) amplitude variations in different scenarios; and (e, f) corresponding SSNR results.

degradation is promptly recovered when the user enters the coverage area of the adjacent WiFi sensing pair. Similar trends are also observed under the cross-room setting shown in Fig. 9c and 9f. However, due to the larger distances between the WiFi sensing nodes, the SSNR overlapping between adjacent nodes is relatively small. These results demonstrate that relying on a single sensing node is insufficient to support reliable, large-area sensing, whereas a distributed deployment of multiple WiFi sensing nodes can effectively complement each other and provide continuous, seamless coverage.

Moreover, although distributed WiFi sensing can provide large sensing coverage, activating all devices simultaneously results in significant resource waste, especially when no user is present within the sensing area of certain sensing nodes. This problem is further exacerbated by the fact that most existing sensing platforms provide insufficient support for simultaneous sensing and communication. Specifically, when the sensing functionality is activated, the communication function is either disabled or suffers from significant performance degradation. These limitations reveal the need for resource-efficient control mechanisms to optimize the performance of large-scale WiFi sensing systems.

Lessons Learned. These results highlight three key insights: (1) multiple sensing links can coexist within the same physical space with highly heterogeneous sensing quality, which cannot be captured by coarse room-level abstraction. (2) Human movement across rooms is continuous, requiring smooth transitions rather than discrete switching. (3) A distributed deployment of WiFi sensing nodes combined with a user-aware handover mechanism is necessary to dynamically select high-quality links, maintain sensing continuity, and improve resource efficiency. These insights motivate the design of an adaptive *ScHO* framework.

4 System Design

4.1 Overview: Design Goals and Approach

Fig. 11 illustrates the overview of our system. The goal of our design is to maintain sensing continuity as a subject moves across different coverage zones among WiFi sensors. By adaptively monitoring and transitioning to the optimal serving node, the system can achieve broader sensing coverage and improved resource efficiency.

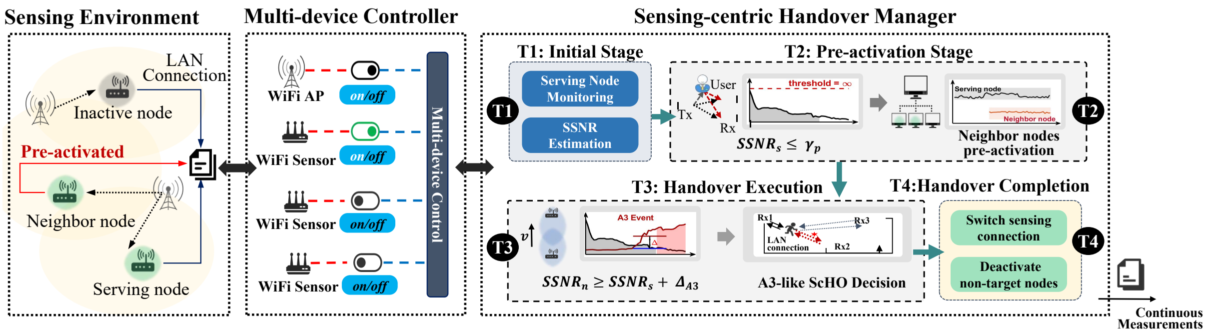

Fig. 10. *ScHO* system pipeline. The system consists of two main components: the sensing-centric handover manager and the multi-device controller. By coordinating sensing link monitoring, proactive pre-activation, and handover execution, the system maintains sensing continuity under user mobility.

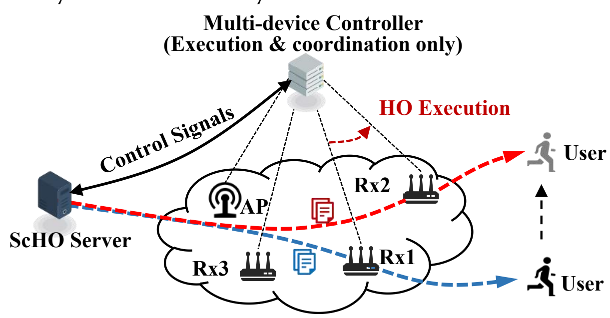

Fig. 11. Centralized network-controlled *ScHO* architecture. The *ScHO* server performs centralized handover decision-making, while the multi-device controller manages device activation/deactivation across distributed sensor nodes (SNs).

Specifically, the *ScHO* system primarily consists of two key components: the *ScHO manager* and the *multi-device controller*. The *ScHO* manager serves as the core control unit of the system. It manages the entire workflow of the *ScHO* process. The second main component, the multi-device controller, receives instructions from the *ScHO* Manager and remotely controls the activation states of all WiFi sensors.

As illustrated in Fig. 10, the system pipeline starts with the multi-device controller activating the initial serving sensor and collecting the channel samples from the serving node. The channel measurements are then received by the *ScHO* manager to assess the sensing quality. Once the sensing quality drops below the pre-handover threshold, the *ScHO* manager sends a command to the multi-device controller to pre-activate the neighboring nodes of the serving node. When the *ScHO* trigger condition is satisfied, the *ScHO* manager compares the SSNR across the neighboring nodes and selects the one with the best sensing quality as the target node. Afterwards, the multi-device controller releases the sensing resources of all nodes other than the target node. The system repeats the aforementioned steps.

4.2 Centralized Network-Controlled Handover Manager

To maintain continuous and high-quality WiFi sensing across large-scale deployments, we design a *ScHO* manager that coordinates the seamless transfer of sensing responsibility across distributed nodes. Unlike communication-driven handover designs that rely solely on link quality, *ScHO* places sensing performance at the core of its decision to determine the node with the most favorable sensing condition. As illustrated in Fig. 12, the *ScHO* workflow is organized into four stages (T1–T4): *measurement*, *triggering*, *execution*, and *completion*.

Table 2. Comparison of Handover Procedures between Communication-oriented and Sensing-oriented Systems.

Stage	Communication Handover	Sensing-centric Handover
T1: Measurement	UE reports SINR / RSRP to the serving BS	The ScHO server monitors sensing quality (e.g., SSNR) of the serving node
T2: Preparation	Serving BS selects the target BS and initiates HO request	Pre-activate neighbors and monitor their sensing quality simultaneously
T3: Execution	UE disconnects from the source BS and connects to the target BS	Switches to the target node and disconnects from the source node
T4: Completion	UE reconfigures and resumes data transfer	System reconfigures and resumes sensing tasks

- ***T1: Measurement and Reports.*** During this stage, the serving node performs continuous channel measurement sampling and forwards the measurements to the *ScHO* server. When pre-activated neighbors are available, their measurements are forwarded to the server simultaneously. This stage focuses solely on sensing data acquisition and quality estimation, forming the input to subsequent triggering and decision stages.
- ***T2: Handover Trigger.*** Based on the channel state measurements received from T1, the *ScHO* server monitors the temporal evolution of the sensing quality. When the serving node's quality drops below the pre-activation threshold, the server invokes the proactive handover mechanism. The pre-activation threshold is set to an infinite value to keep pace with the user's movement. Once the sensing-centric A3-event condition is satisfied, the server raises a handover trigger. This stage is responsible for detecting quality degradation and initiating events that prepare the system for handover. For more information on the *ScHO* triggering mechanism, please refer to Sec. 3.
- ***T3: Handover Execution***. When the A3 condition is satisfied, the server issues a handover command to the multi-device controller, specifying the target node and the corresponding sensing configuration. After receiving the handover command, the multi-device controller triggers the shutdown scripts on the remote sensing nodes. All non-target nodes, including the former serving node and the unselected neighbors, are then switched from sensing mode to normal communication mode.
- ***T4: Handover Completion***. After all non-target nodes have reverted to communication mode, the *ScHO* manager updates the serving-node state in the management module and synchronizes the internal sensing context. Residual resources and obsolete quality records associated with the previous serving node are cleared to prevent interference with subsequent evaluations. The system then transitions the new serving node into steady-state sensing by reinitializing its sliding evaluation window and restoring continuous measurement streaming. Because all candidate nodes were pre-activated in earlier stages, this completion phase introduces minimal latency and maintains uninterrupted sensing. After state synchronization, *ScHO* returns to the measurement stage, closing the handover loop.

Compared with conventional communication-oriented handover mechanisms, one of the key differences lies in the triggering conditions depend on sensing quality. Specifically, traditional handover approaches focus on maximizing the communication quality, while our approach aims to achieve optimal sensing performance. Another key difference in the handover operation is the pre-activation mechanism that proactively activates candidate receivers before the actual handover occurs. This design accounts for the intrinsic startup latency of WiFi sensing systems, where sensing operations are activated only when needed.

4.3 Distributed Multi-Device Control Mechanism

To support sensing-centric handover across distributed WiFi sensor nodes, the *ScHO* system relies on a lightweight and flexible Multi-Device Controller. This component is responsible for managing the operational state of

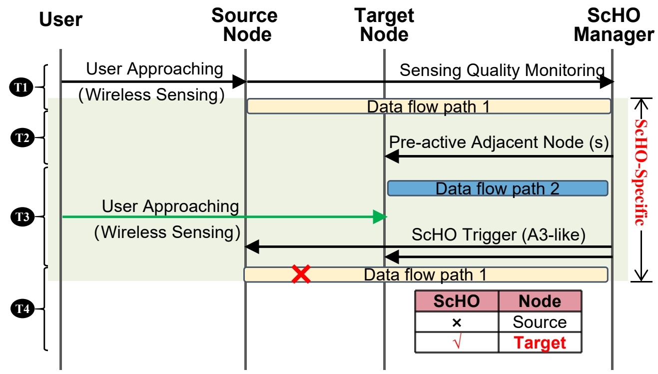

Fig. 12. Sequence diagram of the *ScHO* handover procedure. The red-highlighted components indicate ScHO-specific mechanisms, including sensing-aware triggering and proactive pre-activation.

heterogeneous WiFi sensing devices, including turning nodes on/off and issuing runtime control commands. While not directly involved in sensing or decision-making, it forms the essential infrastructure layer that enables scalable and adaptive sensing across multiple zones.

The multi-device controller operates in a distributed manner by invoking control scripts deployed on distributed devices to coordinate device-level operations. Each device-side script communicates with the controller through lightweight control protocols (*i.e.*, SSH, HTTP), providing a unified interface for managing diverse hardware. This interface accommodates hardware heterogeneity and supports rapid deployment across different devices. By decoupling sensing logic from device control, the multi-device controller offers a scalable and maintainable foundation for real-world deployment of large-scale sensing systems. Note that although the controller is currently implemented on a specific platform (*i.e.*, picoscenes [18]), the proposed modular design naturally supports cross-platform compatibility. By encapsulating platform-specific commands within separate control scripts, the sensing logic remains unchanged across different devices.

It should be noted that the proposed software architecture is scalable and extensible. In particular, adding new WiFi sensors only requires deploying the device-side agent and registering the node at the server. This process does not require any changes to the existing sensing logic. Moreover, the *ScHO* manager is implemented as a set of modular components, allowing new sensing metrics, decision policies, or learning-based models to be plugged in without changing the underlying control framework. This decoupled and centralized design enables *ScHO* to scale to larger deployments and support diverse sensing applications with minimal engineering effort.

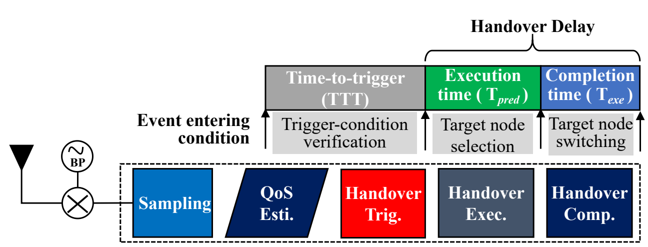

Fig. 13. Timing structure of the *ScHO* process.

(a) Layout. (b) Deployment. (c) Hardware configuration.

Fig. 14. Experiment setup of *ScHO*.

5 Evaluation & Analysis

In this section, we conduct a comprehensive evaluation of *ScHO* using a real-world prototype. We assess the system performance across diverse environmental settings and operational conditions to validate its robustness and efficiency. The handover performance of *ScHO* is quantified by three standard metrics [39]:

(1) The *handover failure ratio* $R_{\text{HOF}} = \frac{N_{\text{HOF}}}{N_{\text{HO}}}$: A failed handover is identified when the executed handover decision mismatches the ground truth. This metric reflects the reliability of the handover strategy.
(2) The *Ping-Pong rate* $R_{\text{pp}} = \frac{N_{\text{pp}}}{N_{\text{HO}}}$: The Ping-Pong handover is recorded when the system switches back to the original serving node within a short time window. A high PPR implies frequent interruptions to the ongoing sensing link.
(3) The *handover delay* $T_{\text{HO}} = T_{\text{end}} - T_{\text{start}}$: The handover delay is defined as the time interval between the *ScHO* trigger (*i.e.*, A3-like event) and the successful re-association to the target node. This metric reflects the timeliness of the handover execution.

Finally, to demonstrate the versatility of *ScHO*, we conduct three case studies: step-frequency estimation, fall detection, and respiration monitoring, covering representative regression and classification tasks.

5.1 Handover Performance Evaluation

5.1.1 Experimental Setup. We prototype *ScHO* using commodity mini-PCs, each equipped with an Intel 5300 wireless NIC, and a ThinkPad laptop that serves as the *ScHO* controller. A typical Intel 5300 network interface card costs approximately \$4–\$6, and a compact miniPC platform costs around \$100–\$500. In our implementation, the system involves up to six miniPCs (one transmitter and multiple receivers). In our experiments, we place the transmitter approximately at the geometric center of the three receivers and distribute the receivers across the room to enlarge the effective sensing coverage. All WiFi sensors are attached to a local area network (LAN) that connects them to the controller. The controller can join the LAN via either wired Ethernet or WiFi, whereas the mini-PCs access the LAN through wired Ethernet because their wireless interfaces are reserved for sensing and thus cannot maintain data connectivity during sensing. Over this LAN, the controller issues handover commands to coordinate the handover process among multiple sensing links.

We adopt a two-layer software architecture consisting of a centralized HO management server and a set of lightweight device-side agents running on the WiFi sensors. Each WiFi sensor is equipped with custom control scripts that handle sensing mode management, including the platform initiation and termination of CSI acquisition. CSI samples are collected using PicoScenes [18] and streamed to the server over TCP/IP connections. On the server side, we implement a real-time *ScHO* manager in Python 3.8, building on an open-source CSI parsing library [38]. The manager maintains persistent control channels to all WiFi sensors, dispatches sensing tasks, and orchestrates the handover workflow. When a handover event arises, the server concurrently acquires sensing data from the current node and its neighboring candidate nodes by remotely executing the corresponding scripts. The resulting CSI streams are continuously fed into a processing pipeline that parses, buffers, and preprocesses the data on the *ScHO* server.

Our experiments are conducted in a home-like environment consisting of three adjacent rooms (denoted as Room A, Room B, and Room C) with different furniture arrangements. We recruit 8 participants (5 males and 3 females) aged between 19 and 28, with heights ranging from 160 cm to 183 cm. Each participant repeats predefined trajectory 5 times. During the experiments, each participant wears a body-mounted accelerometer sensor, which continuously records inertial data. Unless specified, participants follow a default trajectory traversing Room A ⟶ Room B ⟶ Room C (Fig. 22), which corresponds to the node sequence 1 ⟶ 2 ⟶ 3. We use the accelerometer traces to detect and timestamp fall events, and treat these annotated fall segments as the ground truth for evaluating the fall-detection and handover performance of *ScHO*.

5.1.2 Improvement of Sensing Quality & Resource Efficiency. To demonstrate the improvement in sensing quality and resource efficiency enabled by *ScHO*, we evaluate the system using two key metrics: the average SSNR and the Device Redundancy Rate (RR). Specifically, the average SSNR is adopted to quantify overall sensing quality and is defined as $\overline{ssnr} = \frac{1}{T}\sum_{t=1}^{T} ssnr(t)$, where T denotes the total number of sensing time slots. The device redundancy rate quantifies the proportion of time during which more than one sensing device is simultaneously activated, and is defined as RR = $N_{act} - N_{serv}/N_{act}$, where N_{act} denotes the number of activated devices reserved for handover, and N_{serv} denotes the number of devices actually used during handover. All evaluations are conducted on a three-link WiFi sensing testbed.

As illustrated in Fig. 15a, the single-node strategy suffers from fixed link geometry and limited spatial coverage, resulting in a low median SSNR of only 0.048. By contrast, our *ScHO* strategy significantly improves sensing quality by dynamically handing over sensing responsibility to the most informative node, achieving a median SSNR of 0.080, which corresponds to a 1.67× improvement over the single-node baseline. Notably, *ScHO* attains 94.1% of the all-device upper bound (median SSNR of 0.085), where all receivers are kept active concurrently. This result highlights that intelligent handover coordination enables near-optimal sensing fidelity, comparable to a fully active multi-node system, without requiring simultaneous activation of all devices.

However, such performance gains in the multi-node strategy are achieved at the expense of substantial resource overuse. As shown in Fig. 15b, the multi-node approach incurs a high redundancy rate of 0.667, indicating that approximately two-thirds of the sensing hardware remains active while contributing little to effective sensing. In contrast, by selectively activating sensing nodes through handover, *ScHO* significantly reduces unnecessary concurrent operation, maintaining a much lower redundancy rate of 0.373. This corresponds to a 44.1% reduction in redundant active links compared to the multi-node baseline. These results demonstrate that sensing-centric

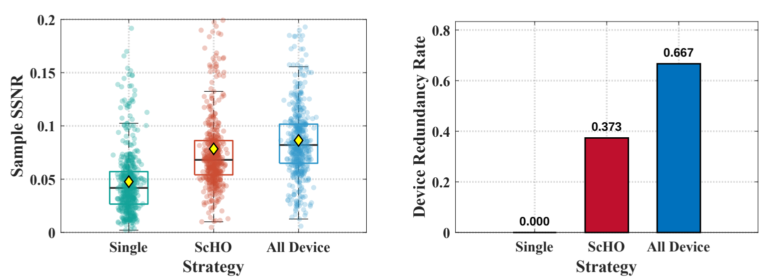

(a) Sensing quality. (b) Redundancy rate.

Fig. 15. Improvement of sensing quality & resource efficiency.

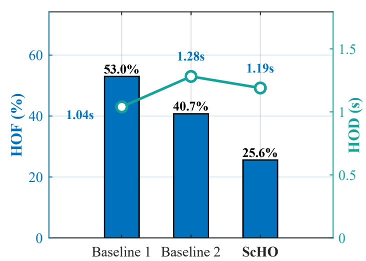

Fig. 16. Comparison of *ScHO* against two baseline schemes in terms of HOF and HOD.

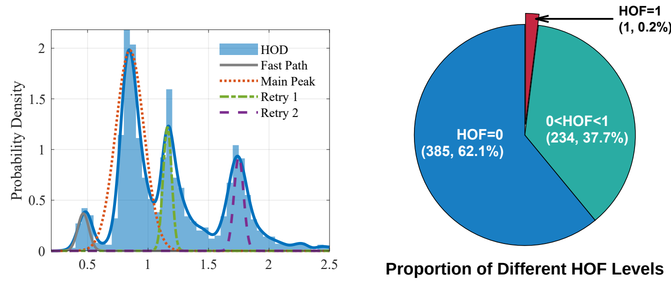

(a) Distribution of HOD.

(b) Trajectory-level HOF.

Fig. 17. Overall handover performance of *ScHO*.

handover not only preserves sensing quality but also substantially improves resource efficiency by reducing redundant node participation.

In sum, within our three-link setup, ScHO enhances sensing quality by 1.67× compared to the single-node approach, while being approximately 1.8× more resource-efficient than the multi-node method. Note that while these numerical gains are reported for a three-node configuration, the advantages of ScHO become increasingly pronounced as the network density grows.

5.1.3 Overall Handover Performance. We first evaluate the overall efficacy of *ScHO* by comparing it against two baseline schemes: Baseline 1 (immediate switching with TTT = 0) and Baseline 2 (no hysteresis with $\Delta_{A3} = 0$). Fig. 16 depicts the comparison results in terms of Handover Failure Rate (HOF) and average latency. As illustrated, *ScHO* significantly outperforms both baselines. While Baseline 1 and Baseline 2 suffer from high failure rates due to frequent, unstable switching (*i.e.*, ping-pong effects) triggered by channel fluctuations, *ScHO* achieves a low HOF of 25.6%, which is computed over all experimental samples, including challenging scenarios with strong interference and varying deployment conditions. Notably, this reliability gain does not come at the cost of responsiveness; *ScHO* maintains an average latency comparable to the aggressive switching of Baseline 1, demonstrating its ability to strike an optimal balance between stability and delay.

To further investigate the temporal characteristics of *ScHO*, we analyze the empirical distribution of handover latency for all handover switches, as shown in Fig. 17a. Unlike a simple Gaussian distribution, the latency exhibits a distinct multi-modal pattern, revealing the underlying operation of our handover protocol. The first minor peak ($\approx$ 0.47 s) corresponds to the Fast Path executions, while the dominant central peak ($\approx$ 0.85 s) represents the standard processing latency. The subsequent tailing peaks ($\approx$ 1.60 s and 1.75 s) are attributed to the retransmission mechanisms (Retries) triggered by temporary channel contention. Despite this multi-peak behavior, the latency remains well-bounded between 0.40 s and 2.60 s, confirming that *ScHO* ensures predictable timeliness even when retransmissions occur.

Finally, to gain deeper insights into the reliability of continuous sensing, we examine the handover performance from a trajectory-level perspective. Fig. 17b reports the distribution of HOF levels across all tested trajectories, which span varying lengths from 2 to 12 nodes. Specifically, 62.1% of trajectories are seamless (HOF = 0), while 37.7% fall into the intermediate range (0 < HOF < 1), where transient degradation occurs but the switch eventually succeeds. Only a negligible fraction (0.2%) of cases result in failure (HOF = 1). These results collectively validate that *ScHO* ensures high reliability for continuous sensing tasks while keeping latency consistently low.

5.1.4 Impact of Hysteresis Threshold (Δ_{A3}). The hysteresis threshold (Δ_{A3}) directly affects the trade-off between handover responsiveness and stability. To quantify its impact, we sweep Δ_{A3} from 0 to 0.50 and evaluate the

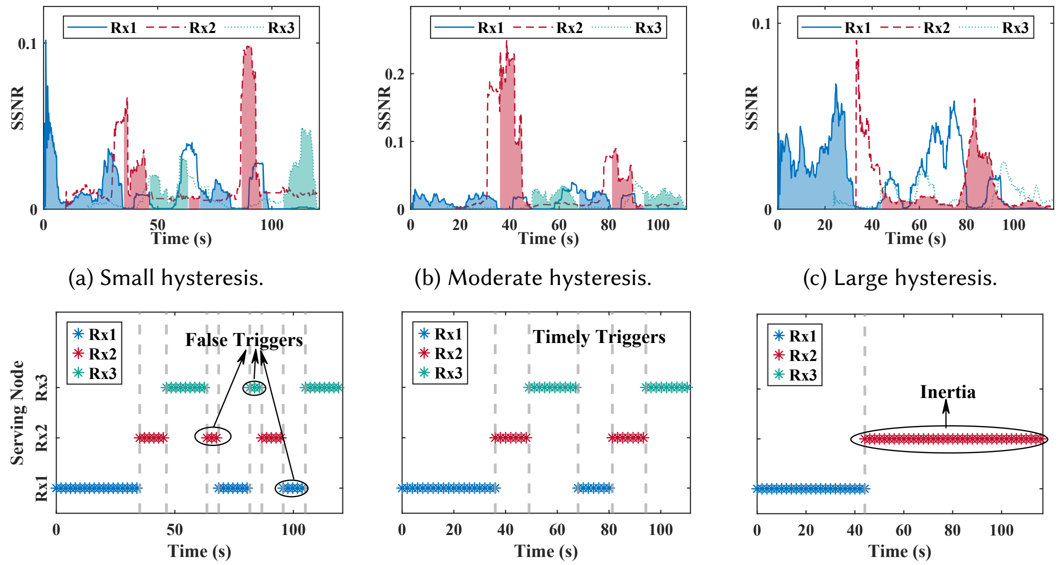

(a) Small hysteresis. (b) Moderate hysteresis. (c) Large hysteresis.

(d) Small hysteresis. (e) Moderate hysteresis. (f) Large hysteresis.

Fig. 18. Handover behaviors resulting from (a) small ($\Delta_{A3} = 0.00$), (b) moderate ($\Delta_{A3} = 0.02$), and (c) large hysteresis thresholds ($\Delta_{A3} = 0.08$).

resulting handover performance. We first analyze the handover behaviors qualitatively. Fig. 18 visualizes the SSNR fluctuations and corresponding handover behaviors under representative thresholds. Specifically, a negligible hysteresis ($\Delta_{A3} = 0.00$, Fig. 18a and 18d) renders the system overly sensitive to instantaneous channel variations. This aggressive setting induces frequent *False Triggers*, where the system oscillates between nodes even when the signal gain is marginal. Conversely, a large hysteresis ($\Delta_{A3} = 0.08$, Fig. 18c and 18f) introduces significant *Inertia*. In this regime, the system clings to a sub-optimal serving node long after a candidate node has exhibited superior quality, resulting in delayed switching. A moderate setting ($\Delta_{A3} = 0.02$, Fig. 18b and 18e) achieves *Timely Triggers*, effectively filtering out small-scale fading while accurately tracking the long-term mobility trend.

These qualitative observations are supported by the quantitative results in Fig. 19. As shown in Fig. 19c, the HOF exhibits a convex relationship with respect to Δ_{A3}. The lowest HOF of 11.8% is achieved at $\Delta_{A3} = 0.02$. When the threshold is reduced to $\Delta_{A3} = 0$, the HOF increases to 23.7%, indicating instability caused by excessive triggering.

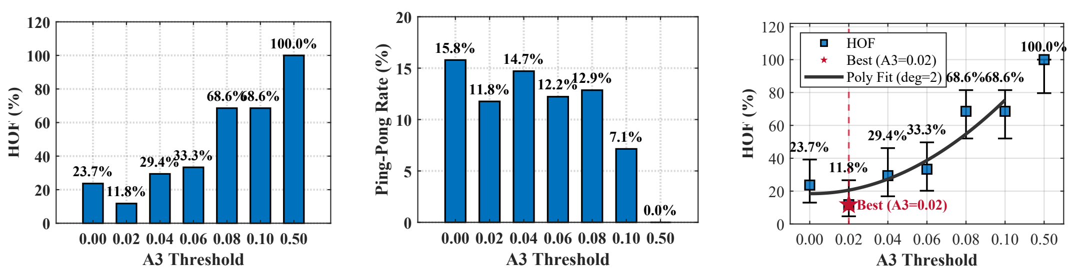

(a) Handover failure rate. (b) Ping-Pong Rate. (c) HOF.

Fig. 19. Impact of A3 event threshold.

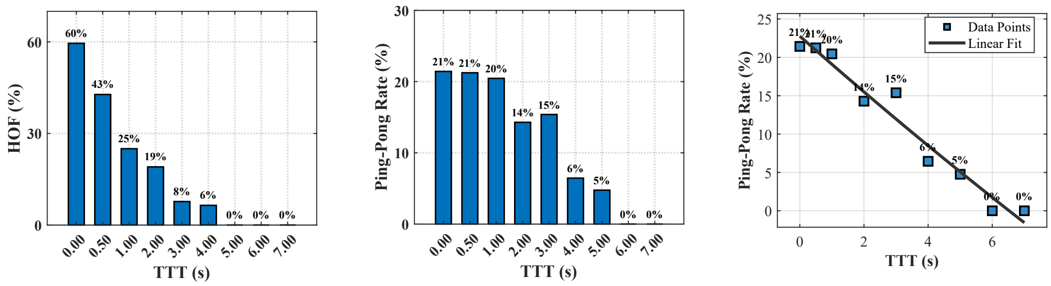

(a) Handover failure rate. (b) Ping-Pong Rate. (c) TTT vs. Ping-Pong Rate.

Fig. 20. Impact of TTT parameter.

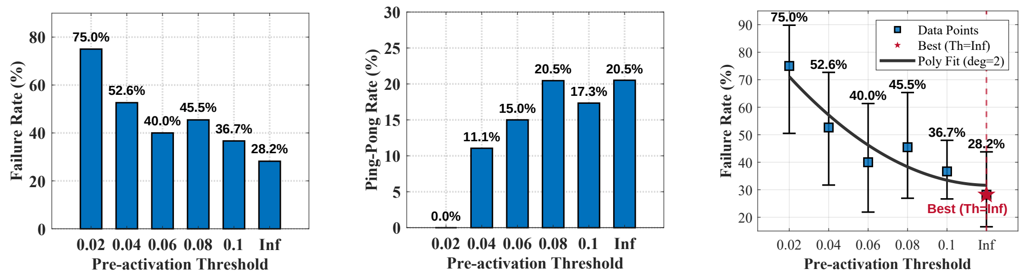

(a) Handover failure rate. (b) Ping-Pong Rate. (c) Pre-activation threshold vs. HOF.

Fig. 21. Impact of Pre-activation Threshold.

Conversely, larger hysteresis values lead to a rapid increase in HOF (e.g., 68.6% at $\Delta_{A3} = 0.08$), suggesting that excessive hysteresis prevents handovers from being completed before link degradation. Regarding stability, Fig. 19b shows that the Ping-Pong Rate decreases monotonically as Δ_{A3} increases, from 15.8% at $\Delta_{A3} = 0$ to 7.1% at 0.10. Based on this trade-off, $\Delta_{A3} = 0.02$ is selected as the operating point, as it achieves the lowest HOF while maintaining a reasonable level of handover stability.

5.1.5 Impact of Time-To-Trigger (TTT). To investigate the temporal sensitivity of *ScHO*, we conduct a sensitivity study on the TTT parameter by sweeping TTT $\in \{0, 0.5, 1, 2, 3, 4, 5\}$s while keeping all other settings fixed. Figure 20a depicts the impact of TTT on the Handover Failure Ratio (HOF). The results indicate that the HOF exhibits a monotonic decrease as TTT increases. Specifically, with a negligible TTT (TTT = 0 s), the system suffers from a high failure rate of 60%. As TTT extends to 3.00 s, the HOF significantly drops to 8%. When TTT $\geq$ 5.00 s, the failures are completely eliminated (HOF = 0%). However, it is worth noting that simply maximizing TTT is not feasible. Although a large TTT (e.g., 7.00 s) achieves zero failures in our trace, it introduces the *Too-Late Handover* problem. In this case, the system clings to a deteriorating serving link for an excessive duration before triggering the handover, which degrades the user experience despite the eventual success of the switch.

Figs. 20b and 20c reveal a linear correlation between TTT and the ping-pong rate. With TTT = 0s, the ping-pong rate reaches 80%, while increasing TTT progressively suppresses oscillatory handovers (down to 15% at 3 s and near 0% at 5 s). The linear fit in Fig. 20c further confirms that TTT effectively acts as a temporal low-pass filter, rejecting transient superiority events that would otherwise trigger back-and-forth switching. Considering both HOF and ping-pong behaviors, TTT $\approx$ 2 s provides a balanced operating point in our setting.

5.1.6 Impact of Pre-activation Threshold (γ_p). To study the sensitivity of *ScHO* to the pre-activation mechanism, we evaluate system performance under different pre-activation thresholds (γ_p), ranging from 0.02 to infinity (Inf).

Table 3. HOF and ping-pong rate (PPR) across repeated traversal cycles on the $1 \rightarrow 2 \rightarrow 3$ loop, grouped by N mod 3.

Metric	Residue (N mod 3)	Loop 1	Loop 2	Loop 3	Loop 4
HOF	$N \equiv 0 \pmod 3$	–	36.36%	24.39%	13.79%
	$N \equiv 1 \pmod 3$	25.00%	15.38%	13.40%	8.70%
	$N \equiv 2 \pmod 3$	33.33%	9.09%	21.15%	10.29%
PPR	$N \equiv 0 \pmod 3$	–	36.36%	24.39%	6.89%
	$N \equiv 1 \pmod 3$	0.00%	15.38%	11.80%	7.35%
	$N \equiv 2 \pmod 3$	33.33%	6.06%	9.61%	1.47%

The threshold acts as a wake-up condition that determines when a neighboring device is activated in advance. As illustrated in Fig. 21a, the HOF exhibits a sharp decline as the threshold increases. Specifically, a low threshold (e.g., 0.02) results in a prohibitive HOF of 75.0%.

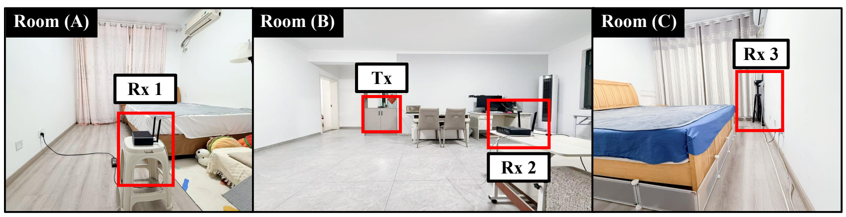

Fig. 22. Experiment setup with 3 adjacent rooms.

To assess the statistical reliability of this trend, Fig. 21c further reports the failure rate with Wilson 95% confidence intervals. The fitted curve and the clear separation between the confidence intervals of low (0.02–0.04) and higher threshold settings indicate that the degradation observed at small thresholds is statistically significant. One likely explanation is that an overly restrictive threshold delays the activation of adjacent devices, preventing them from entering the sensing state in time and causing the system to miss the handover window. Fig 21b further shows that the Ping-Pong Rate (PPR) remains at 0.0% under these small thresholds. This absence of Ping-Pong behavior, however, should not be interpreted as improved stability. Instead, it reflects a lack of responsiveness, where the neighboring device fails to activate and the handover process is never fully initiated, precluding oscillatory connections.

5.1.7 Impact of Trajectory Length. We evaluate *ScHO* under different trajectory lengths by varying the number of nodes a user traverses along a predefined path. We adopt a looped trajectory ($1 \rightarrow 2 \rightarrow 3$) to obtain longer trajectories within a fixed deployment, where each traversal cycle incrementally extends the trajectory length. The sensing configuration and handover parameters are kept fixed, while only the trajectory length L is varied. Fig. 23a shows that HOF is higher for short trajectories, revealing a clear *cold-start vulnerability*. When $L \leq 3$, the failure rate remains elevated (*e.g.*, 25.0% at L=1, 33.3% at L=2, and peaking at 36.4% at L=3). This degradation is mainly due to the long initialization time in the early stage of a trial. Specifically, with limited observations, the delayed device activation and insufficient samples can reduce handover accuracy. As L increases, the system accumulates more reliable temporal evidence, and HOF generally decreases and becomes stable (*e.g.*, dropping to 15.4% at L=4 and 9.1% at L=5, and staying low for longer trajectories). This trend is closely correlated with the Ping-Pong behavior. As illustrated in Fig. 23b, the PPR can be extremely high at some short-to-mid lengths (reaching up to 36.4%), but it gradually decreases and stabilizes (often within 1.5% $\sim$ 24.4%) as the trajectory becomes longer. Finally, Fig. 23c indicates that HOD becomes lower and less variable as L increases.

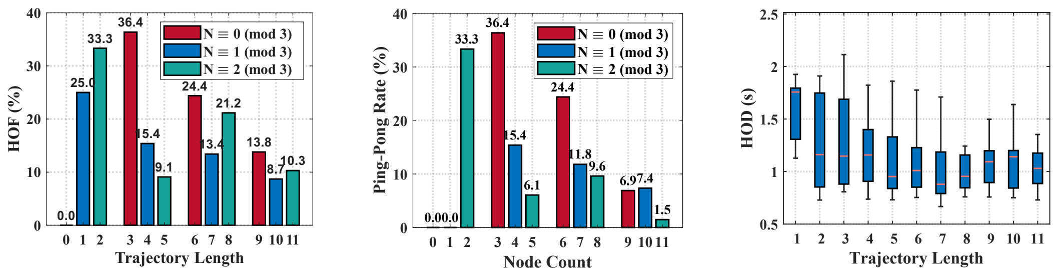

(a) Handover failure rate.

(b) Ping-Pong Rate.

(c) Handover delay.

Fig. 23. Impact of trajectory length.

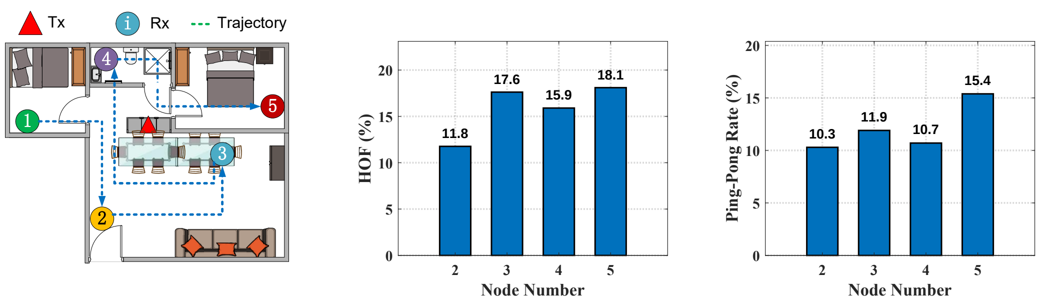

(a) Experimental Setup.

(b) Handover failure rate.

(c) Ping-Pong Rate.

Fig. 24. Impact of number of nodes.

Tab. 3 further illustrates the impact of trajectory length by reporting the HOF and PPR across repeated traversal cycles on the $1 \longrightarrow 2 \longrightarrow 3$ loop, grouped by N mod 3. The results show that both HOF and PPR generally decrease as the traversal cycle progresses. In the first loop, the system consistently exhibits high failure and instability, especially for N=0 and N=2, where HOF exceeds 30% and PPR reaches up to 36.4%. This observation aligns with the *cold-start effect* identified earlier, where the sensing and handover pipeline has not yet stabilized after activation, resulting in higher failure and oscillation rates.

5.1.8 Impact of Number of Nodes. To evaluate the scalability of *ScHO* under different network densities, we investigate its performance by varying the number of receiver-associated sensing links N from 2 to 5. Fig. 24b illustrates the impact of node count on the HOF. We observe that as N increases from 2 to 5, the HOF slightly rises from 11.8% to 18.1%, with intermediate values of 17.6% and 15.9% for $N = 3$ and $N = 4$, respectively. Notably, the failure rate does not exhibit a monotonic or sharp increase beyond 3 nodes, remaining within a comparable and stable range. This non-linear trend occurs because each handover event is mainly affected by locally available neighboring links rather than all deployed nodes. Despite the increase in the total number of nodes, such that each handover event involves only a limited set of local candidate links. Therefore, *ScHO* scales to denser multi-node deployments without substantial degradation in handover performance.

The impact on handover stability is shown in Fig. 24c. The ping-pong rate increases from 10.3% for $N = 2$ to 15.4% for $N = 5$. This trend reflects higher switching sensitivity in denser deployments, where more competing links are available for selection, increasing the likelihood of transient link superiority. However, the ping-pong

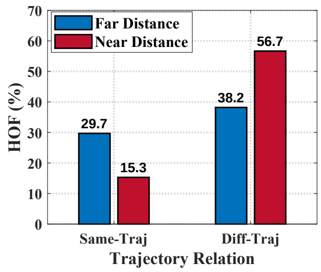

(a) Handover failure rate.

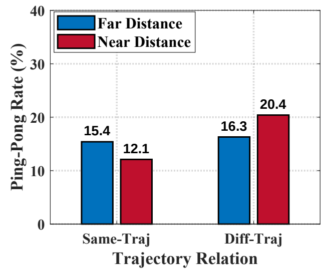

(b) Ping-Pong rate.

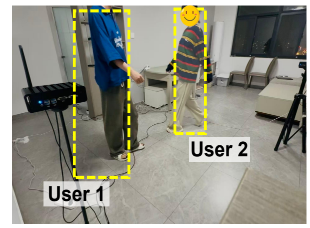

(c) Experimental setup.

Fig. 25. Impact of multiple users.

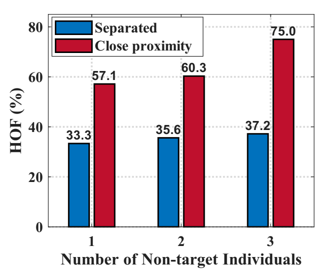

(a) Handover failure rate.

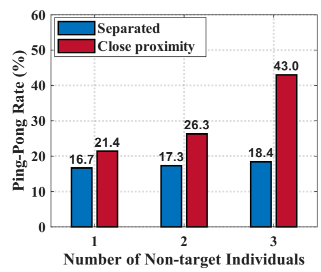

(b) Ping-Pong rate.

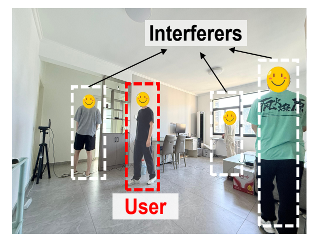

(c) Experimental setup.

Fig. 26. Impact of motion interference from non-target individuals.

rate remains well controlled, reaching around 10.7% at $N = 4$, which demonstrates that *ScHO*'s temporal filtering mechanism effectively suppresses excessive oscillations even in multi-link clusters.

5.1.9 Impact of Multi-Users Scenarios. To evaluate the performance of *ScHO* under multi-user scenarios,we consider two-user scenarios where users follow either the same trajectory or different trajectories. In the same-trajectory case, the two users sequentially traverse the path $1 \longrightarrow 2 \longrightarrow 3$, one following the other. In the different-trajectory case, one user follows the path $1 \longrightarrow 2 \longrightarrow 3$, while the other follows a different route, $1 \longrightarrow 3 \longrightarrow 2$. Both near and far spatial separations are considered to emulate typical indoor activities. As shown in Fig. 25a and Fig. 25b, *ScHO* maintains stable performance when the two users follow the same trajectory. In this case, the handover failure ratio decreases from 29.7% under far separation to 15.3% under near separation, while the ping-pong rate remains relatively low, decreasing from 15.4% to 12.1%. This indicates that when users move coherently, the dominant sensing link for the target user remains stable, and additional reflections do not significantly disrupt the handover process.

In contrast, the *different trajectory* condition is more challenging, particularly when the users are closely located. In this case, the handover failure ratio and ping-pong rate increase significantly, reaching up to 56.7% and 20.4%, respectively. This degradation suggests that independently moving nearby users introduce stronger cross-interference through multiple dynamic reflections, which perturbs the SSNR profile and reduces the stability of the decision boundary between candidate sensing links. This limitation may be alleviated in future WiFi systems, where increased bandwidth and larger antenna arrays can provide higher spatial resolution, improving the ability to distinguish and separate multiple users.

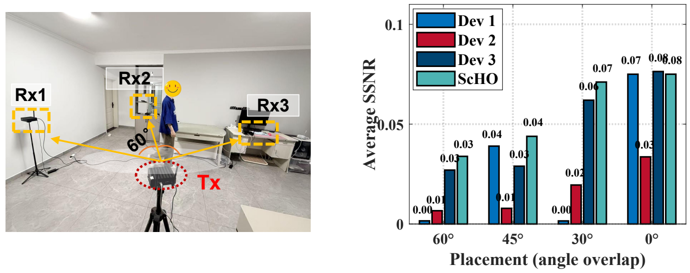

(a) Experimental setup. (b) Improvement of sensing quality.

Fig. 27. Impact of overlapping areas.

5.1.10 Impact of Non-target Motion Interference. To evaluate the robustness of *ScHO* under non-target motion interference, we consider multiple non-target individuals under two spatial configurations, *i.e.*, *separated* and *close proximity*, while varying their number from 1 to 3. Under the *separated* configuration, their trajectories are spatially separated from the target's trajectory. Under the *close proximity* configuration, they move near the target and introduce stronger interference into the active sensing links. The target user follows a predefined trajectory across nodes 1 ⟶ 2 ⟶ 3, while the non-target individuals perform walking activities in the sensing environment. As shown in Fig. 26a and Fig. 26b, *ScHO* maintains relatively stable handover performance under the *separated* configuration. As the number of non-target individuals increases, the HOF ratio increases only slightly from 33.3% to 37.2%, with the ping-pong rate increasing from 16.7% to 18.4%. This indicates that when the non-target motion occurs far from the active sensing links, the system can effectively perform handover decisions in the presence of non-target motion interference.

In contrast, the *close proximity* configuration results in more pronounced performance degradation. As the number of non-target individuals increases from 1 to 3, the HOF ratio increases from 57.1% to 75.0%, while the ping-pong rate increases from 21.4% to 43.0%. This performance degradation suggests that a nearby moving body introduces strong motion interference, which perturbs the SSNR profile and introduces ambiguity between candidate links. As a result, the SSNR variations of the candidate links may be dominated by non-target motion rather than the target user, leading the system to select suboptimal links and exhibit frequent oscillatory handover decisions. This limitation could be alleviated by incorporating spatial filtering techniques to suppress non-target signal components when the sensing system is capable of distinguishing signals from different users.

5.1.11 Impact of Overlapping Areas. To examine the performance of *ScHO* under varying degrees of multi-link coverage, we evaluate its sensing quality by adjusting the spatial overlap among sensing links. As shown in Fig. 27a, we vary the angular separation among three sensing devices (60°, 45°, 30°, and 0°) while fixing the

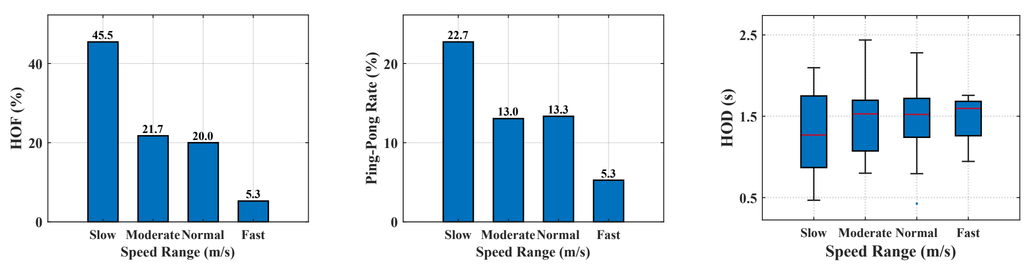

(a) Handover failure rate. (b) Ping-Pong Rate. (c) Handover delay.

Fig. 28. Impact of user speed.

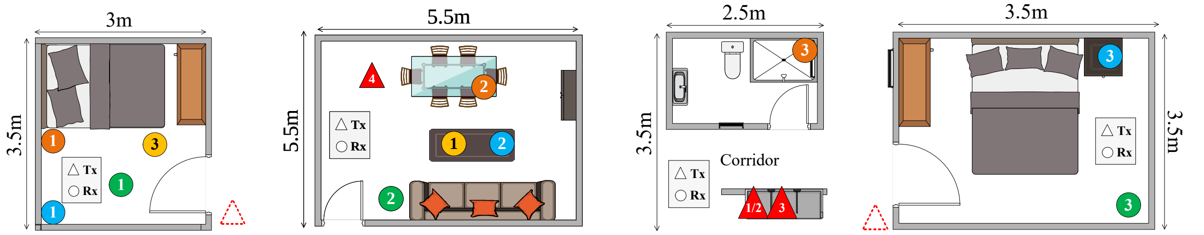

(a) Bedroom 1. (b) Living room. (c) Bathroom. (d) Bedroom 2.

Fig. 29. Deployment of four sensing configurations spanning four adjacent rooms. The specific placement strategies are distinguished by color, where numbers indicate the device ID.

Line-of-Sight (LoS) length of each link at 2 m. Smaller angular separations correspond to larger overlapping regions, with 0° representing a nearly co-located extreme case. In each trial, the participant remains within the common overlapping region and performs natural movements for 2 minutes. We conduct 10 independent trials for each configuration to calculate the average SSNR.

Fig. 27b illustrates the sensing quality performance under these overlapping conditions. It can be observed that *ScHO* consistently achieves higher SSNR than any individual sensing link across all configurations. For instance, at a 45° separation, *ScHO* yields an SSNR of approximately 0.04, representing a 33% improvement over the best individual link (Dev 3) and a 300% improvement over the lowest-performing link (Dev 2). This demonstrates that *ScHO* can effectively mitigate the impact of low-quality links by dynamically selecting or transitioning to higher-quality sensing channels. As the overlapping area increases (from 60° to 0°), the average SSNR of *ScHO* rises from 0.035 to 0.08. This is because higher overlap constrains user activities closer to the LoS of all links, minimizing signal degradation among all sensing links.

5.1.12 Impact of User Moving Speed. To evaluate the robustness of *ScHO* under different user moving speeds, we vary the user speed from 0.5 m/s to 1.8 m/s. We categorize the trials into four qualitative levels based on average walking speed: *Slow*, *Moderate*, *Normal*, and *Fast*. The instantaneous speed is estimated from the body-mounted accelerometer using a step-frequency–based method [29].

Fig. 28a illustrates the HOF across different speed bins. We observe a distinct *"Low-Velocity Vulnerability"*. Specifically, the HOF peaks at 45.5% in the *Slow* bin, which is nearly an order of magnitude higher than that in the *Fast* bin (5.3%). This degradation is mainly due to the *prolonged dwell time* in spatially overlapping sensing regions. Specifically, in indoor environments, the sensing coverage of adjacent nodes inevitably overlaps, creating "confusion zones" where signals from multiple sensing links are ambiguous. When a user moves slowly,

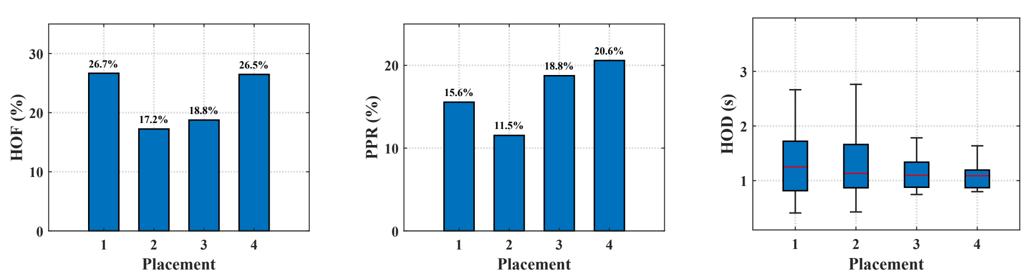

(a) Handover failure rate. (b) Ping-Pong Rate. (c) Handover delay.

Fig. 30. Impact of device placement.

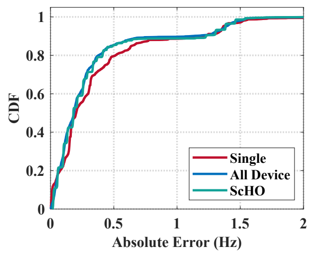

(a) CDF of walking speed error.

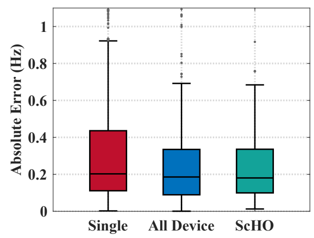

(b) Error distribution.

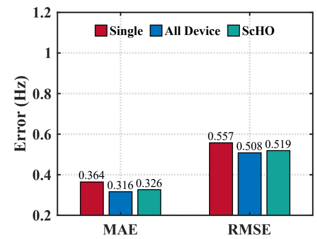

(c) Overall metrics.

Fig. 31. Performance comparison of walking speed estimation.

the extended residence time in these overlapping regions *exacerbates* the system's confusion, increasing the likelihood of making incorrect handover decisions. In contrast, higher speeds allow the user to traverse these overlapping regions rapidly. This effectively minimizes the duration of ambiguity, thereby suppressing the oscillatory handovers to a negligible level (5.3% in the *Fast* bin). This performance degradation is intrinsically linked to the Ping-Pong Effect, as depicted in Fig. 28b. Moreover, Fig. 28c shows that while the central tendency of HOD remains relatively stable across bins, the variance differs noticeably.

5.1.13 Impact of Device Placement. We further investigate the impact of device placement by testing four placement configurations across four adjacent rooms, as illustrated in Fig. 29. Each configuration corresponds to a distinct spatial arrangement of sensing devices within a room. The same color across different rooms denotes the same placement configuration, while the numbers indicate individual device indices. Fig. 30 shows the HOF under the four placement configurations. We observe that handover performance varies across different placements. Placement 2 achieves the lowest HOF (17.2%), while Placements 1 and 4 exhibit higher failure rates, with Placement 4 reaching 26.5%. Fig. 30b reports the Ping-Pong Rate for the same configurations. Placement 4 shows a higher Ping-Pong Rate (20.6%) compared to Placements 2 and 3, which exhibit lower oscillation levels. This suggests that certain placement layouts are more prone to ambiguous sensing outcomes, increasing the likelihood of oscillatory handovers. Fig. 30c further shows the distribution of Handover Delay (HOD) across the four placements. The median HOD remains similar across configurations, with only modest variation in dispersion. This indicates that device placement has limited impact on handover execution latency once a handover is triggered. Overall, these results indicate that device placement can influence handover reliability and stability under real-world conditions.

5.2 Application-level Evaluation

We further evaluate the effectiveness of *ScHO* from an application-level perspective. Three case studies are conducted to demonstrate the performance gains of *ScHO* in practical sensing scenarios.

5.2.1 Case I: Walking Speed Estimation. We first evaluate *ScHO* through a walking speed estimation case study, where users move naturally within an indoor environment while performing continuous walking activities. Walking speed, represented by step frequency, is estimated from time-series CSI amplitude measurements. Ground truth is obtained using a wearable IMU, where a step-based pedestrian dead reckoning (PDR) algorithm detects step events and computes step frequency for performance benchmarking.

We formulated walking speed estimation as a time-series regression problem. CSI amplitude sequences are first processed using a low-pass Butterworth filter with a cutoff frequency of 3 Hz, followed by Z-score normalization. The processed CSI data is segmented into sliding windows of 10 seconds with a step size of 2 seconds. A convolutional recurrent neural network with an attention mechanism is employed to map CSI measurements to step frequency. The same network configuration is used for all sensing strategies.

We compare three sensing strategies:

- *Single Device:* walking speed estimation using a fixed sensing link.
- *All Devices:* fusion of features from all available links without selection.
- *ScHO (Ours):* adaptive sensing handover that dynamically selects the most informative link.

These configurations capture two representative sensing paradigms in existing systems: fixed single-link sensing and multi-link sensing. They provide a practical basis for evaluating the effectiveness of sensing-centric handover under user mobility.

Fig. 31 and Tab. 4 summarize the quantitative results of walking speed estimation. When a single fixed sensing link is used, the estimation error is the highest, with an MAE of 0.364 Hz and an RMSE of 0.557 Hz. This degradation is mainly caused by the limited sensing coverage of a static link. When all available links are jointly exploited, the estimation accuracy improves, achieving an MAE of 0.316 Hz and an RMSE of 0.508 Hz. The use of multiple links increases the probability that at least one link maintains favorable sensing conditions throughout the walking process. By contrast, *ScHO* dynamically performs sensing-oriented handover, selecting the most informative link as the user moves. This strategy achieves an MAE of 0.326 Hz and an RMSE of 0.519 Hz, closely approaching the performance of the multi-device configuration while activating only a single sensing link at any time. Compared with the single-device strategy, *ScHO* reduces the MAE by approximately 10.4%.

Table 4. Comparison of Walking Speed Estimation Performance (MAE & RMSE)

Method	**Input Channels**	**MAE (Hz)**	**RMSE (Hz)**	**MAE Improv.**
Single-Device	1	0.364	0.557	-
All-Devices	3	0.316	0.508	+13.2%
***ScHO* (Ours)**	**1 (Dynamic)**	**0.326**	**0.519**	**+10.4%**

The error distributions in Fig. 31a and Fig. 31b further illustrate the robustness of *ScHO*. *ScHO* effectively suppresses large estimation errors and achieves a median error and interquartile range comparable to those of the multi-device strategy, confirming that sensing-oriented handover successfully avoids the sensing blind spots caused by user mobility.

5.2.2 Case II: Fall Detection. We evaluate *ScHO* through a fall detection case study that targets large-area and mobile sensing scenarios, where users naturally move within an indoor environment. In such scenarios, users are not confined to a fixed position but naturally walk, turn, and relocate within the environment, causing the effective sensing link to change continuously over time. Experiments were conducted in a controlled environment where subjects performed a sequence of activities, including walking, interspersed with simulated fall events on soft mats. The ground truth labels (Fall vs. Walk) were manually annotated and synchronized with the CSI timestamps via body-mounted ACC sensor. Similar sensing configurations are adopted as in case I, including single-device sensing, multi-device all-on sensing, and the proposed *ScHO* with sensing-centric handover.

We formulate fall detection as a binary classification problem. The system processes time-series CSI amplitude data to distinguish between "Fall" and "Walk". The raw CSI data undergoes preprocessing including low-pass filtering (3 Hz cutoff) and Z-score normalization. To capture the abrupt and transient signal patterns induced by fall events, we adopt a lightweight deep learning model that integrates local feature extraction, adaptive channel reweighting, and temporal modeling. Specifically, a 1D ResNet encoder is used to extract high-level motion features from noisy CSI signals, while embedded Squeeze-and-Excitation blocks emphasize discriminative subcarriers and suppress static multipath interference. A Bidirectional GRU further models the temporal context

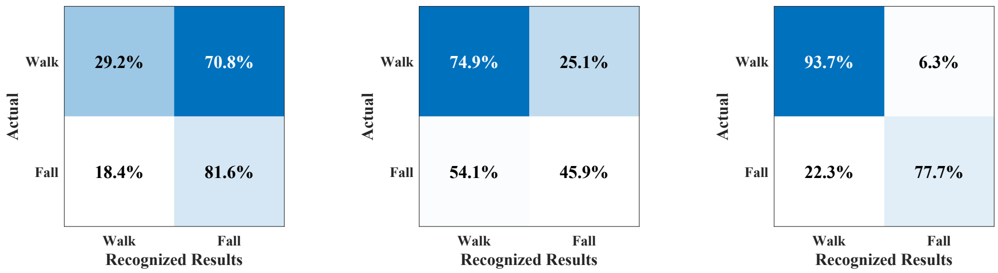

(a) Single device. (b) All devices. (c) *ScHO*.

Fig. 32. Performance comparison of fall detection.

before and after a fall, enabling the network to capture rapid state transitions. The resulting features are fed into a sigmoid-based classification head. To account for the severe class imbalance between falls and daily activities, a weighted cross-entropy loss is employed to penalize missed fall events more heavily during training.

Table 5. Comparison of Fall Detection Performance

Method	Accuracy	Precision	Recall	F-Measure	AUC
Single Device	37.13%	18.24%	**81.79%**	29.06%	50.70%
All Devices	70.32%	38.91%	46.37%	42.31%	55.05%
***ScHO* (Ours)**	**91.12%**	**70.88%**	77.73%	**73.75%**	**92.62%**

Tab. 5 and Fig. 32 summarize the quantitative results of the fall detection experiment under three sensing strategies. The results reveal fundamentally different sensing behaviors and illustrate how sensing-oriented handover improves robustness under user mobility. We note that these results are obtained under a challenging wide-area deployment involving multi-room trajectories and NLoS conditions, where signal attenuation and multipath interference significantly degrade sensing quality compared to controlled environments. When fall detection is performed using a single fixed sensing link, the system achieves a relatively high recall of 81.79%, but suffers from extremely low precision of 18.24% and accuracy of 37.13%. This degradation primarily stems from the limited effective sensing range of a single link. As the user moves within a large area, they frequently walk out of the reliable sensing region of the fixed link.

Additionally, when all available links are activated and jointly exploited, the overall accuracy improves to 70.32%, yet recall drops significantly to 46.37%. This behavior arises because the sensing model is primarily optimized for single-link input. In the multi-device baseline, signals from multiple links are combined using a simple aggregation strategy, which may dilute discriminative features and obscure the transient patterns associated with fall events. By contrast, *ScHO* dynamically performs sensing-oriented handover, selecting the most informative link as the user moves. This strategy achieves an accuracy of 91.12% and an AUC of 0.926, while improving precision to 70.88% and maintaining a robust recall of 77.73%. The resulting F-measure of 73.75% demonstrates that *ScHO* enables reliable fall detection over an extended sensing area without activating all sensing links. These results highlight that the key advantage of *ScHO* lies in maintaining continuous sensing reliability across user movement, rather than optimizing peak performance at a fixed location.

5.2.3 Case III: Respiration Rate Monitoring. We further evaluate *ScHO* through a respiration rate monitoring case study, which aims to assess fine-grained sensing performance under realistic indoor scenarios. In such scenarios, users move naturally across different coverage areas of WiFi sensors and remain stationary near certain sensing area for short periods, during which respiration monitoring can be performed. We follow the respiration rate

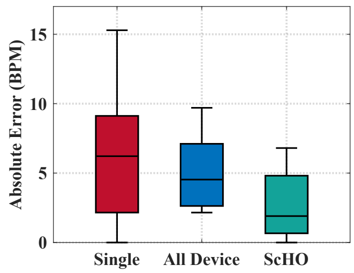

(a) Error distribution.

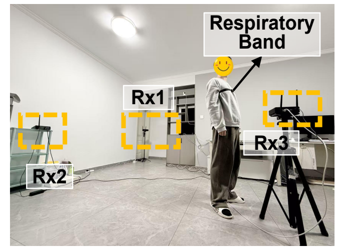

(b) Experimental setup.

Fig. 33. Performance comparison of respiration rate estimation.

estimation method in [45], and employ Fast Fourier Transform (FFT) algorithm to estimate the respiration rate (*i.e.*, breaths per minute, bpm) using the collected CSI samples. The MAE is defined as the error between ground truth and estimated rate to quantify the respiration monitoring performance. The ground truth is recorded by Bigrun Team Respiratory Belt logger sensor. For evaluation, we only extract respiration data corresponding to resting periods, where respiration signals are not affected by walking motion.

Table 6. Comparison of Respiration Rate Estimation Performance (MAE & RMSE).

Method	**Input Channels**	**MAE (BPM)**	**RMSE (BPM)**	**MAE Improv.**
Single-Device	1	7.78	9.07	-
All-Devices	3	6.17	6.92	+20.7%
ScHO (Ours)	**1 (Dynamic)**	**4.78**	**6.20**	**+38.6%**

Tab. 6 and Fig. 33a illustrate the performance of different configurations for respiration rate monitoring. Overall, ScHO achieves the best performance, followed by the multi-device configuration, while the single-link setup performs the worst. Specifically, when a single fixed sensing link is used, the estimation error is the highest, with an MAE of 7.78 BPM. This is mainly due to its limited sensing coverage and high sensitivity to environmental dynamics. The multi-device configuration improves the estimation accuracy by averaging the results from three sensing devices, reducing the MAE to 6.17 BPM. This improvement comes from the increased likelihood that at least one link operates under favorable sensing conditions. In contrast, ScHO dynamically performs sensing-oriented handover to select the most informative link, achieving the lowest MAE of 4.7 BPM. Unlike simple averaging, this approach incorporates the most informative links, thereby mitigating noise and destructive interference. These results demonstrate that, for fine-grained sensing tasks such as respiration monitoring, selecting the optimal sensing link yields better performance.

6 Related Works

Handover Mechanisms. Handover has been extensively studied in wireless communication systems, particularly in cellular and Wi-Fi networks[24, 37]. Many existing handover mechanisms aim to maintain connectivity continuity by monitoring reference signal received power (RSRP) [19], signal-to-noise ratio (SNR) [7], or estimated link quality [7, 35]. Advanced approaches leverage mobility prediction [6, 34, 51] or multi-path transmission protocols like Multipath TCP (MPTCP) [36, 49] to improve handover performance and reduce service disruption. While these methods effectively address connection-level stability, they are designed primarily for data transmission continuity and have not considered the continuity of sensing services that rely on consistent physical-layer signal patterns. In contrast, our work focuses on a sensing-centric handover paradigm, where the goal is to maintain sensing quality and service continuity during device switches under mobility.

WiFi Sensing. WiFi sensing has gained significant attention as a key enabler of ubiquitous perception in next-generation networks. Prior works have explored various techniques to extract sensing features from channel state information (CSI) [14, 16, 25], beamforming feedback information (BFI) [3, 13], or Doppler signatures [32, 57]. By analyzing variations in wireless signals, WiFi sensing has been widely explored for various applications, including human activity recognition [14, 15, 25], gesture detection [33, 43], vital signs [5, 9, 13, 44], *etc.* However, most of these systems assume a static sensing platform or fixed deployment, without addressing the challenges that arise when users move across different coverage areas. Our work complements these studies by addressing sensing service continuity under mobility through sensing-centric handover.

Multi-Device Coordination for WiFi Sensing. Recent studies have explored the use of multiple sensors to improve sensing accuracy and spatial coverage [53, 55]. CrossSense [55] presents a deep-learning framework that aggregates CSI measurements from multiple access points to enable cross-site human activity sensing[60, 61]. By leveraging spatial diversity, it significantly improves sensing generalization across different environments. More recently, SleepMore [53] leverages signals from multiple ambient Wi-Fi devices to infer users' sleep duration across large residential deployments, showing the promise of multi-device sensing in real-world, longitudinal scenarios. While these systems demonstrate the benefits of sensing coordination across multiple devices, they do not tackle the challenge of how to maintain a continuous sensing session when the user moves across the coverage areas of different devices. In contrast, our work focuses on the sensing-centric handover problem, proposing metrics and algorithms to enable online device switching that preserves sensing quality and minimizes service disruption.

7 Discussion and Future Work

In this section, we discuss the limitations of the current implementation and outline directions for future research to further enhance the scalability and robustness of *ScHO*.

Hardware Latency and System Robustness. We also identify a practical limitation regarding the device startup latency. Due to the constraints of the underlying firmware on our experimental platform, the initialization of the sensing state requires a relatively long time window. This hardware-induced latency increases the penalty for handover failures. If a device fails to wake up in time, it may cause a "chain reaction" of missed detections, leading to continuous errors in subsequent state estimation. Although we cannot modify the closed-source firmware at this stage, we anticipate that future optimizations in WiFi sensing driver support and hardware capabilities will mitigate this initialization overhead, thereby allowing our handover algorithm to achieve even higher responsiveness and stability.

Trajectory-based Selective Activation. Currently, our pre-activation mechanism adopts a conservative strategy by waking up all potential adjacent nodes once a user approaches the boundary. While this ensures that the target device is ready for handover, it inevitably introduces energy redundancy. In future work, we plan to integrate user trajectory prediction into the handover logic. By leveraging historical movement patterns to predict the user's destination, the system can selectively wake up only the most probable target node. This refinement would significantly reduce energy consumption and channel contention, making the system more scalable for large-scale deployments with dense sensor networks.

On-node Sensing Quality Estimation. In the current architecture, the assessment of sensing quality (e.g., report generation) is performed centrally at the server. While effective for prototyping, this centralized approach imposes a heavy burden on network communication and server-side computation, especially when scaling to multi-user scenarios. To address this, we aim to push the "sensing intelligence" to the edge. By migrating the lightweight quality estimation modules to the sensing nodes (APs), devices can self-evaluate their sensing capability and only transmit high-level status updates or condensed features to the server. This distributed approach will minimize bandwidth usage and reduce the latency of the decision-making loop.

Link Selection Strategy and Multi-Link Extension. The current design of *ScHO* adopts a single-link sensing strategy, where only the most reliable link is selected at each time instance for sensing. This design serves as a lightweight yet effective solution for maintaining continuous sensing coverage across spatial regions. However, for more complex activity recognition tasks, relying on a single CSI stream may limit the ability to capture rich spatial dynamics, especially in scenarios involving fine-grained motion patterns, multi-person interactions, or occlusion-prone environments. In such cases, incorporating information from multiple sensing links can provide complementary observations and improve robustness against signal blockage and environmental variability.

ISAC Extensibility and Practical Constraints. The proposed framework already supports sensing-centric handover through CSI-driven link quality estimation and coordinated multi-node operation. However, in current implementations, sensing nodes operating in CSI extraction mode do not support simultaneous communication, and the handover process is coordinated over a wired Ethernet network to ensure stable and low-latency operation. Nevertheless, the framework can be naturally extended to integrated sensing and communication (ISAC), as the underlying logic of sensing-centric handover is fundamentally compatible with emerging ISAC protocols (e.g., IEEE 802.11bf). Furthermore, with the introduction of next-generation WiFi chipsets that provide dedicated support for sensing, the limitation of traffic-dependent CSI acquisition will be alleviated, enabling stable and continuous sensing alongside communication.

8 Conclusion

In this paper, we present *ScHO*, a sensing-centric handover system that enables continuous WiFi sensing under user mobility by dynamically transferring sensing responsibility among multiple WiFi sensing nodes according to sensing quality. *ScHO* integrates a centralized sensing-oriented control plane, an SSNR-based handover trigger metric with theoretical boundary characterization, and a proactive, A3-like handover mechanism that jointly addresses sensing instability and handover latency in practical deployments. Extensive real-world experiments with multiple commodity WiFi sensing nodes demonstrate that *ScHO* achieves a 1.67× improvement in median sensing quality compared to single-node sensing, while reaching 94.1% of the multi-node upper-bound performance that keeps all devices active simultaneously. At the same time, *ScHO* significantly improves resource efficiency by reducing redundant active sensing links by 44.1%, effectively balancing sensing fidelity and system overhead through selective handover. By transforming handover from a communication-oriented operation into a sensing-driven, quality-aware coordination mechanism, *ScHO* provides a practical and scalable solution for mobility-aware WiFi sensing. These results show that high-quality continuous sensing can be achieved without relying on fully active multi-node operation, making *ScHO* a key step toward energy-efficient, large-scale, and deployable WiFi sensing systems.

9 Acknowledgements

This work is supported by National Natural Science Foundation of China (Grant No. 62302145, No. 62422213, No. 62372149, and No. U23A20303), Beijing Nova Program (20240484641), Major Scientific and Technological Project of Anhui Provincial Science and Technology Innovation Platform (Grant No. 202305a12020012), Key Laboratory of Space-Air-Ground Integrated Network Security, Ministry of Industry and Information Technology, Shandong Key Laboratory of Advanced Computing, and Fundamental Research Funds for the Central Universities (Grant No. JZ2025HGTB0225).

References

[1] 3rd Generation Partnership Project (3GPP). 2017. *Further Advancements for E-UTRA Physical Layer Aspects*. Technical Report 3GPP TR 36.814. 3GPP. https://www.3gpp.org/ftp/Specs/archive/36_series/36.814/ V9.0.0.

[2] 3rd Generation Partnership Project (3GPP). 2019. Evolved Universal Terrestrial Radio Access (E-UTRA) and Evolved Universal Terrestrial Radio Access Network (E-UTRAN); Overall description; Stage 2. 3GPP TS 36.300, Version 15.7.0. https://www.3gpp.org/ftp/Specs/archive/36_series/36.300/

[3] Siyu Chen, Hongbo Jiang, Jingyang Hu, Zhu Xiao, and Daibo Liu. 2024. Silent thief: Password eavesdropping leveraging Wi-Fi beamforming feedback from POS terminal. In *IEEE INFOCOM 2024-IEEE Conference on Computer Communications*. IEEE, 321–330.

[4] Feng-Qi Cui, Jinyang Huang, Sirui Zhao, Kun Li, Zhi Liu, Meng Li, Ziyu Jia, Dan Guo, and Meng Wang. 2026. PersoMoni: A Comprehensive Video-Based Benchmark Dataset for Fine-grained Personality Assessment with 15 Trait Dimensions. *IEEE Transactions on Affective Computing* (2026), 1–14. doi:10.1109/TAFFC.2026.3698795

[5] Feng-Qi Cui, Anyang Tong, Jinyang Huang, Jie Zhang, Meng Li, Xin Yan, Linsheng Huang, Dan Guo, and Meng Wang. 2026. Towards Trustworthy Dynamic Facial Expression Recognition via Information Bottleneck Modeling. *IEEE Transactions on Information Forensics and Security* (2026).

[6] Merim Dzaferagic, Bruno Missi Xavier, Diarmuid Collins, Vince D'Onofrio, Magnos Martinello, and Marco Ruffini. 2024. Ml-based handover prediction over a real o-ran deployment using ran intelligent controller. *IEEE Transactions on Network and Service Management* (2024).

[7] Nada A Ezz-Eldien, Mohamed F Abdelkader, Mahmoud I Abdalla, and Heba M Abdel-Atty. 2020. Handover performance improvement in heterogeneous wireless network. In *2020 11th IEEE Annual Information Technology, Electronics and Mobile Communication Conference (IEMCON)*. IEEE, 0821–0830.

[8] Yuanrun Fang, Fu Xiao, Biyun Sheng, Letian Sha, and Lijuan Sun. 2022. Cross-scene passive human activity recognition using commodity WiFi. *Frontiers of Computer Science* 16, 1 (2022), 161502.

[9] Yao Ge, Ahmad Taha, Syed Aziz Shah, Kia Dashtipour, Shuyuan Zhu, Jonathan Cooper, Qammer H Abbasi, and Muhammad Ali Imran. 2022. Contactless WiFi sensing and monitoring for future healthcare-emerging trends, challenges, and opportunities. *IEEE Reviews in Biomedical Engineering* 16 (2022), 171–191.

[10] Zhengxin Guo, Wenyang Yuan, Linqing Gui, Biyun Sheng, and Fu Xiao. 2023. BreatheBand: A fine-grained and robust respiration monitor system using WiFi signals. *ACM Transactions on Sensor Networks* 19, 4 (2023), 1–18.

[11] Yinghui He, Jianwei Liu, Mo Li, Guanding Yu, and Jinsong Han. 2024. Forward-Compatible Integrated Sensing and Communication for WiFi. *IEEE Journal on Selected Areas in Communications* (2024).

[12] Yinghui He, Jianwei Liu, Mo Li, Guanding Yu, Jinsong Han, and Kui Ren. 2023. Sencom: Integrated sensing and communication with practical wifi. In *Proceedings of the 29th Annual International Conference on Mobile Computing and Networking*. 1–16.

[13] Jingyang Hu, Hongbo Jiang, Tianyue Zheng, Jingzhi Hu, Hongbo Wang, Hangcheng Cao, Zhe Chen, and Jun Luo. 2024. M 2-Fi: Multi-person Respiration Monitoring via Handheld WiFi Devices. In *IEEE INFOCOM 2024-IEEE Conference on Computer Communications*. IEEE, 1221–1230.

[14] Huakun Huang, Peiliang Wang, Lingjun Zhao, Zeyang Dai, Guowei Liu, and Honghao Gao. 2025. WiPE: Privacy-friendly WiFi-based Human Pose Estimation on Consumer Platform. *IEEE Transactions on Consumer Electronics* (2025).

[15] Jinyang Huang, Yuanhao Feng, Feng-Qi Cui, Xiang Zhang, Zhi Liu, Xin Liu, Jianchun Liu, Fusang Zhang, and Meng Li. 2026. Identifying Who You Are No Matter What You Write through Abstracting Handwriting Style. *IEEE Transactions on Dependable and Secure Computing* (2026), 1–15.

[16] Jinyang Huang, Bin Liu, Chenglin Miao, Xiang Zhang, Jianchun Liu, Lu Su, Zhi Liu, and Yu Gu. 2023. Phyfinatt: An undetectable attack framework against phy layer fingerprint-based wifi authentication. *IEEE Transactions on Mobile Computing* 23, 7 (2023), 7753–7770.

[17] IEEE 802.11 Task Group bf. 2025. IEEE P802.11bf: WLAN Sensing. https://www.ieee802.org/11/Reports/tgbf_update.htm. Accessed: 2025-04-08.

[18] Zhiping Jiang, Tom H Luan, Xincheng Ren, Dongtao Lv, Han Hao, Jing Wang, Kun Zhao, Wei Xi, Yueshen Xu, and Rui Li. 2021. Eliminating the barriers: Demystifying Wi-Fi baseband design and introducing the PicoScenes Wi-Fi sensing platform. *IEEE Internet of Things Journal* 9, 6 (2021), 4476–4496.

[19] Michail Kalntis, George Iosifidis, José Suárez-Varela, Andra Lutu, and Fernando A Kuipers. 2026. Meta-Learning-Based Handover Management in NextG O-RAN. *IEEE Journal on Selected Areas in Communications* (2026).

[20] Raja Karmakar, Georges Kaddoum, and Samiran Chattopadhyay. 2022. Mobility management in 5G and beyond: A novel smart handover with adaptive time-to-trigger and hysteresis margin. *IEEE Transactions on Mobile Computing* 22, 10 (2022), 5995–6010.

[21] Edward Kasner and Fred Supnick. 1943. The Apollonian packing of circles. *Proceedings of the National Academy of Sciences* 29, 11 (1943), 378–384.

[22] Haoyang Li, Zhiwen Yu, Yixuan Luo, Helei Cui, and Bin Guo. 2024. ContinuousSensing: A Task Allocation Algorithm for Human–Robot Collaborative Mobile Crowdsensing with Task Migration. *CCF Transactions on Pervasive Computing and Interaction* 6, 3 (2024), 228–243.

[23] Xinyu Li, Yuanhao Cui, J Andrew Zhang, Fan Liu, Daqing Zhang, and Lajos Hanzo. 2022. Integrated human activity sensing and communications. *IEEE Communications Magazine* 61, 5 (2022), 90–96.

[24] Yun Li, Bin Cao, and Chonggang Wang. 2016. Handover schemes in heterogeneous LTE networks: challenges and opportunities. *IEEE Wireless Communications* 23, 2 (2016), 112–117.

[25] Guiping Lin, Weiwei Jiang, Sicong Xu, Xiaobo Zhou, Xing Guo, Yujun Zhu, and Xin He. 2022. Human activity recognition using smartphones with WiFi signals. *IEEE Transactions on Human-Machine Systems* 53, 1 (2022), 142–153.

[26] Fan Liu, Yuanhao Cui, Christos Masouros, Jie Xu, Tony Xiao Han, Yonina C Eldar, and Stefano Buzzi. 2022. Integrated sensing and communications: Toward dual-functional wireless networks for 6G and beyond. *IEEE journal on selected areas in communications* 40, 6 (2022), 1728–1767.

[27] Sicong Liu, Bin Guo, Ziqi Wang, Lehao Wang, Zimu Zhou, Xiaochen Li, and Zhiwen Yu. 2025. DeepSwarm: Towards Swarm Deep Learning with Bi-Directional Optimization of Data Acquisition and Processing. *Frontiers of Computer Science* 19, 3 (2025), 193501.

[28] Dongming Luan, En Wang, Wenbin Liu, Yongjian Yang, and Jing Deng. 2025. Stability-Aware Data Offloading Optimization in Edge-Based Mobile Crowdsensing. *Frontiers of Computer Science* 19, 11 (2025), 1911503.

[29] Yang Lv, Wen Zhang, Xiaoxu Zhang, and Jian Xu. 2024. Hip-knee motion-lagged coordination mapping enables speed adaptive walking for powered knee prosthesis. *IEEE Transactions on Neural Systems and Rehabilitation Engineering* (2024).

[30] Dongliang Ma, Zhuo Sun, Zhiqiang Wei, Yifan Guo, Yangqian Lei, Zhu Wang, Zhiwen Yu, and Bin Guo. 2025. AdaptTrack: A Robust Tracking System for Complex Environments Based on WiFi Device Selection Strategy. *Proceedings of the ACM on Interactive, Mobile, Wearable and Ubiquitous Technologies* 9, 3 (2025), 1–29.

[31] Xuanqi Meng, Weiping Ge, Yichen Tian, Xinyu Tong, Xiulong Liu, Xin Xie, and Wenyu Qu. 2025. Metatrack: Enabling wi-fi device free tracking in complex scenarios. *Proceedings of the ACM on Interactive, Mobile, Wearable and Ubiquitous Technologies* 9, 4 (2025), 1–26.

[32] Xuanqi Meng, Jiarun Zhou, Xiulong Liu, Xinyu Tong, Wenyu Qu, and Jianrong Wang. 2023. Secur-Fi: A secure wireless sensing system based on commercial Wi-Fi devices. In *IEEE INFOCOM 2023-IEEE Conference on Computer Communications*. IEEE, 1–10.

[33] Kai Niu, Fusang Zhang, Xuanzhi Wang, Qin Lv, Haitong Luo, and Daqing Zhang. 2021. Understanding WiFi signal frequency features for position-independent gesture sensing. *IEEE Transactions on Mobile Computing* 21, 11 (2021), 4156–4171.

[34] Syed Maaz Shahid, Jee-Hyeon Na, and Sungoh Kwon. 2024. Incorporating Mobility Prediction in Handover Procedure for Frequent-handover Mitigation in Small-Cell Networks. *IEEE Transactions on Network Science and Engineering* (2024).

[35] Sachin Sharma, Saptarshi Ghosh, Manav Bhatnagar, and BK Panigrahi. 2024. Power Efficient Handoff Management in Hybrid V2X Communication: Game-Theoretic Approach to Resource Allocation with Load Reduction. *IEEE Transactions on Mobile Computing* (2024).

[36] Hassan Sinky, Bechir Hamdaoui, and Mohsen Guizani. 2016. Proactive multipath TCP for seamless handoff in heterogeneous wireless access networks. *IEEE Transactions on Wireless Communications* 15, 7 (2016), 4754–4764.

[37] Şafak Sönmez, Ibraheem Shayea, Sajjad Ahmad Khan, and Abdulraqeb Alhammadi. 2020. Handover management for next-generation wireless networks: A brief overview. *2020 IEEE Microwave Theory and Techniques in Wireless Communications (MTTW)* 1 (2020), 35–40.

[38] City Su. 2019. *csiread: A Python parser for Channel State Information (CSI) of Intel, Atheros, and Nexmon.* https://github.com/citysu/csiread

[39] Kai Sun, Qingfeng Han, Zongchang Yang, Wei Huang, Haijun Zhang, and Victor CM Leung. 2025. Proactive Handover Type Prediction and Parameter Optimization Based on Machine Learning. *IEEE Transactions on Wireless Communications* (2025).

[40] Kai Sun, Jiarun Yu, Wei Huang, Haijun Zhang, and Victor CM Leung. 2021. A multi-attribute handover algorithm for QoS enhancement in ultra dense network. *IEEE Transactions on Vehicular Technology* 70, 5 (2021), 4557–4568.

[41] Renrui Tan, Tu Hong, Yichen Tian, Xinyu Tong, Sheng Chen, Xiulong Liu, Xin Xie, and Wenyu Qu. 2025. Wimap: Autonomous wi-fi mapping for device-free tracking in smart homes. *Proceedings of the ACM on Interactive, Mobile, Wearable and Ubiquitous Technologies* 9, 4 (2025), 1–23.

[42] Chenjun Tang, Wei Sun, Xing Zhang, Jin Zheng, Jian Sun, and Chongpei Liu. 2023. A sequential-multi-decision scheme for WiFi localization using vision-based refinement. *IEEE Transactions on Mobile Computing* 23, 3 (2023), 2321–2336.

[43] Dazhuo Wang, Jianfei Yang, Wei Cui, Lihua Xie, and Sumei Sun. 2022. AirFi: Empowering WiFi-based passive human gesture recognition to unseen environment via domain generalization. *IEEE Transactions on Mobile Computing* 23, 2 (2022), 1156–1168.

[44] Meng Wang, Jinyang Huang, Xiang Zhang, Zhi Liu, Meng Li, Peng Zhao, Huan Yan, Xiao Sun, and Mianxiong Dong. 2024. Target-oriented wifi sensing for respiratory healthcare: from indiscriminate perception to in-area sensing. *IEEE Network* (2024).

[45] Xuanzhi Wang, Kai Niu, Jie Xiong, Bochong Qian, Zhiyun Yao, Tairong Lou, and Daqing Zhang. 2022. Placement matters: Understanding the effects of device placement for WiFi sensing. *Proceedings of the ACM on Interactive, Mobile, Wearable and Ubiquitous Technologies* 6, 1 (2022), 1–25.

[46] Wi-Fi Alliance. 2023. Wi-Fi Alliance Applauds 2023 Wi-Fi CERTIFIED Leaders' Contributions to Wi-Fi. *The Beacon* (December 2023). https://www.wi-fi.org/beacon/the-beacon/wi-fi-alliance-applauds-2023-wi-fi-certified-leaders-contributions-to-wi-fi Accessed: 2024-06-24.

[47] Chenshu Wu, Beibei Wang, Oscar C Au, and KJ Ray Liu. 2022. Wi-Fi can do more: Toward ubiquitous wireless sensing. *IEEE Communications Standards Magazine* 6, 2 (2022), 42–49.

[48] Dan Wu, Youwei Zeng, Ruiyang Gao, Shenjie Li, Yang Li, Rahul C Shah, Hong Lu, and Daqing Zhang. 2021. WiTraj: Robust indoor motion tracking with WiFi signals. *IEEE Transactions on Mobile Computing* 22, 5 (2021), 3062–3078.

[49] Jianpeng Xu and Bo Ai. 2021. Deep reinforcement learning for handover-aware MPTCP congestion control in space-ground integrated network of railways. *IEEE Wireless Communications* 28, 6 (2021), 200–207.

[50] Wei Xu, Zhu Wang, Yifan Guo, Zhihui Ren, Yandi Xu, Bin Guo, Zhiwen Yu, and Xingshe Zhou. 2025. Acoustic Sensing Mechanisms, Technologies, and Applications: A Survey. *CCF Transactions on Pervasive Computing and Interaction* 7, 4 (2025), 522–549.

[51] Wenjun Yang, Lin Cai, Shengjie Shu, and Jianping Pan. 2024. Mobility-aware congestion control for multipath QUIC in integrated terrestrial satellite networks. *IEEE Transactions on Mobile Computing* (2024).

[52] Bozhong Yu, Lili Chen, and Hao Chen. 2024. Multi-Band Metasurface Design for Seamless Communication and Sensing Enhancement. *CCF Transactions on Pervasive Computing and Interaction* 6, 3 (2024), 244–254.

[53] Camellia Zakaria, Gizem Yilmaz, Priyanka Mary Mammen, Michael Chee, Prashant Shenoy, and Rajesh Balan. 2023. Sleepmore: Inferring sleep duration at scale via multi-device wifi sensing. *Proceedings of the ACM on Interactive, Mobile, Wearable and Ubiquitous Technologies* 6, 4 (2023), 1–32.

[54] Youwei Zeng, Dan Wu, Jie Xiong, Enze Yi, Ruiyang Gao, and Daqing Zhang. 2019. FarSense: Pushing the range limit of WiFi-based respiration sensing with CSI ratio of two antennas. *Proceedings of the ACM on Interactive, Mobile, Wearable and Ubiquitous Technologies* 3, 3 (2019), 1–26.

[55] Jie Zhang, Zhanyong Tang, Meng Li, Dingyi Fang, Petteri Nurmi, and Zheng Wang. 2018. CrossSense: Towards cross-site and large-scale WiFi sensing. In *Proceedings of the 24th annual international conference on mobile computing and networking*. 305–320.

[56] Youwei Zhang, Zhi Liu, and Suhua Tang. 2025. VibeAlign: Maximizing V ar i ation of Heart Be at in CSI of COTS Wi-Fi Devices via Signal Align ment. *Proceedings of the ACM on Interactive, Mobile, Wearable and Ubiquitous Technologies* 9, 4 (2025), 1–31.

[57] Leqi Zhao, Rui Xiao, Jianwei Liu, and Jinsong Han. 2024. One is Enough: Enabling One-shot Device-free Gesture Recognition with COTS WiFi. In *IEEE INFOCOM 2024-IEEE Conference on Computer Communications*. IEEE, 1231–1240.

[58] Xiaolong Zheng, Kun Yang, Jie Xiong, Liang Liu, and Huadong Ma. 2024. Pushing the limits of WiFi sensing with low transmission rates. *IEEE Transactions on Mobile Computing* (2024).

[59] Xiaokang Zhou, Wei Liang, I Kevin, Kai Wang, Katsutoshi Yada, Laurence T Yang, Jianhua Ma, and Qun Jin. 2025. Decentralized federated graph learning with lightweight zero trust architecture for next-generation networking security. *IEEE Journal on Selected Areas in Communications* (2025).

[60] Xiaokang Zhou, Wei Liang, Katsutoshi Yada, Laurence T Yang, Zheng Yan, Kenli Li, and Qun Jin. 2026. Variational GAN enhanced causal effect inference for interpretable learning in heterogeneous IoT systems. *IEEE Transactions on Consumer Electronics* (2026).

[61] Xiaokang Zhou, Xuzhe Zheng, Tian Shu, Wei Liang, Kevin I-Kai Wang, Lianyong Qi, Shohei Shimizu, and Qun Jin. 2023. Information theoretic learning-enhanced dual-generative adversarial networks with causal representation for robust OOD generalization. *IEEE Transactions on Neural Networks and Learning Systems* 36, 2 (2023), 2066–2079.